Unlocking exceptional diffusion of porous Ni@SiO$_2$ nanocapsule catalysts for enhanced dry reforming of methane

Zi-Yian Lim [a], Junling Tu [b], Fengling Zhou [b], Baiman Chen [b], Kwang Leong Choy [a],*

[a] *Suzhou Key Laboratory of Advanced Sustainable Materials and Technologies, Division of Natural and Applied Sciences, Duke Kunshan University, Kunshan, Jiangsu 215316, China*
[b] *Guangdong Provincial Key Laboratory of Distributed Energy Systems, School of Chemical Engineering and Energy Technology, Dongguan University of Technology, Dongguan 523808, China*

ABSTRACT

This paper introduces innovative porous Ni@SiO$_2$ nanocapsule catalysts for high-temperature dry reforming of methane, synthesized through a selective etching method in a mild alkaline solution with varying CTAB concentrations. While core-shell catalysts have been proven effective in addressing issues like active metal sintering and coking, their dense inert oxide shells can impede intrinsic kinetics and hinder gas diffusion. The optimized catalyst, M-NSNC-2, showcases exceptional performance, featuring small Ni nanoparticles (5.3 nm) within a porous SiO$_2$ nanocapsule (>900 m^{2}g^{-1}). M-NSNC-2 demonstrates outstanding methane conversion (>82%), stability (50 hours), and resistance to sintering, agglomeration, and higher-ordered carbon deposition. In comparison to dense Ni@SiO$_2$ nanocapsules (NSNC), M-NSNC-2 exhibits superior performance with nearly 13-fold enhanced mass transfer diffusivity. Additionally, the porous Ni@SiO$_2$ nanocapsule catalyst exhibits an apparent CH$_4$ activation energy of 67.9 kJ/mol at a kinetic regime of 1800,000 mL g$_{cat}^{-1}$h^{-1}, emphasizing its efficacy in catalyzing dry reforming of methane.

1. Introduction

The continuous emission of greenhouse gases (mainly CO$_2$) into the atmosphere due to fossil fuel usage poses a severe risk to the global environment that leads to climate change[1]. Also, the ever-growing energy demand of human society has increased the use of conventional fossil fuels to meet their requirement in energy production [2]. For a long-term sustainable approach, transition to renewable energy, and reducing the dependence on fossil fuels, future energy sources must meet sustainable, carbon-free, and renewable[3].

To mitigate the CO$_2$ emissions, a few varieties could be adapted to generate hydrogen or fuel from different sources, such as water electrolysis, methane pyrolysis, and steam methane reforming with carbon capture. Among the ideal options, carbon dioxide removal (CDR) from the air is emerging, demonstrating a few pilot plants globally[4]. Another anthropogenic gas, methane, also poses a great risk for global warming. A study in 2020 showed that the methane growth rate reached 15.1 ± 0.4 parts per billion per year, the highest value since 1984[5]. A recent surge in converting CO$_2$ into intermediate-chemical products such as hydrocarbons and methanol has gained tremendous interest in

the research community[6]. Synthetic gas such as H$_2$ and CO produced from the dry reforming of methane is a potential pathway for producing hydrocarbons and energy storage. It favors various downstream chemical processes, such as Haber[7] and Fischer-Tropsch [8]. However, challenges in the dry reforming of methane, including active metal agglomeration and carbon deposition, causing catalyst deactivation. Therefore, achieving relatively higher activity, stability, and reduced catalyst coking are highly desirable.

Noble metal-based catalysts are primarily used for dry reforming methane, and their high cost is unfavorable for industrial applications [9]. Regarding activity and cost, nickel-based catalysts are the commonly used candidate for the dry reforming of methane. However, major drawbacks for nickel-based catalysts, such as active metal sintering and severe carbon deposition, remain[10]. Fortunately, decades of research in developing nickel-based catalysts have led to more innovative ideas for designing the catalysts[11–13]. The activity of the catalysts is highly dependent on the size and dispersion of the active metal. Also, when the active metal is smaller than 7 nm, it can promote methane dissociation and resist coke formation[14]. Approaches such as doping with other metals [15] (e.g., Rh) or metal oxides[16–18] (e.g.,

ZrO_2, MgO, K_2O) have proven to augment the activity of catalysts owing to their strong-metal support interactions[19] (e.g., $0.1Ni/CeO_2$), surface chemical properties[20] (e.g., Ni/Al_2O_3, Ni/SiO_2), and oxygen vacancy[19] (e.g., CeO_2). Other substrates, such as composite oxides[21, 22] (e.g., $La_{0.9}Sr_{0.1}FeO_3/YSZ$, $Ni-La_2O_3/SiC$) and mesoporous materials [23–25] (e.g., ordered mesoporous $Ni-La_2O_3/Al_2O_3$, Ni-SBA-15, Ni/ZrO_2), are also potential choices for the dry reforming of methane.

Recent innovative approaches such as core-shell and yolk-shell catalysts have proven effective against sintering/agglomeration by enveloping active metal nanoparticles with an inert shell[26–30]. It also proved to be coking resistive by surrounding the active metal nanoparticles (e.g., Ni) inside an inert matrix (e.g., ZrO_2) attributed to the confinement effect[27,31,32]. Additionally, the structures were designed to encapsulate active metal nanoparticles with highly permeable shells to allow efficient reactant gaseous exchange while ensuring that the active metals remained isolated[33]. Lately, a core-shell structured $Ni@SiO_2$ catalyst with small-sized Ni nanoparticles (circa. 5 nm) exhibited sintering-free of Ni and low carbon deposition attributed from the silica shell (circa. 11.3 nm) overlay confined the moving space of Ni nanoparticles and enabling low carbon diffusion ($< 0.7\%$ weight loss) in Ni particles[34]. $Ni@SiO_2$ catalysts continuously catalyzed and exhibited 91% CH_4 and 94% CO_2 conversion at 800 °C, 18,000 $mLg_{cat}^{-1}h^{-1}$ for 50 hours. Another study approached with the incorporation of indium to form a confined indium-nickel intermetallic alloy nanocatalyst ($In_xNi@SiO_2$) showed high performance and stability even after 430 hours[35]. Such stability and performance were due to the confinement effect of a core-shell structure and the enhanced transfer of electrons from indium to nickel in the In-Ni intermetallic alloys. Moreover, it was found that the metallic Ni had a weakened state to activate the C-H bond, resulting in a less cracking process of methane. It ($In_{0.5}Ni@SiO_2$) showed methane conversion of 92% at 800 °C, 18,000 $mLg_{cat}^{-1}h^{-1}$ for 430 hours. Similarly, the $15Ni-SiO_2@SiO_2$ core-shell catalyst exhibited CH_4 and CO_2 conversion of 72.7% and 93%, respectively under 700 °C, $CH_4/CO_2 = 1.5$, 24,000 $mLg_{cat}^{-1}h^{-1}$ for 360 minutes [36]. The exceptional stability and resistance to carbon deposition were ascribed to the robust Ni-SiO_2 interaction and the complete coverage of Ni particles by the SiO_2 shell. This unique configuration led to the formation of a $Ni-SiO_2@SiO_2$ catalyst, effectively inhibiting the migration and sintering of Ni nanoparticles during the reaction.

However, most reported core-shell catalysts are limited to a low-weight hourly space velocity. Until recently, a $Ni@SiO_2$ nanocapsule catalyst (Ni@SNC) was developed and tested at 60,000 $mLg_{cat}^{-1}h^{-1}$[37]. The catalyst has a quasi-zero-dimensional, tubular structure in which inner cavities can be controlled (5.0–13 nm x 5.0–50.0 nm dimensions) via water-in-oil micro-emulsion through different aging times (e.g., 3 h, 6 h, and 12 h). However, the performance of the spherical $Ni@SiO_2$ catalyst was found to be inferior, mainly attributed to the limited reaction space, which caused an over-accumulation of carbon intermediates and inner Ni aggregations. In addition, most spherical $Ni@SiO_2$ have poor structural stability, and their silica shell tends to polymerize and collapse due to the presence of water from reverse water-gas shift reaction[38]. It was suggested that the inner cavity of Ni@SNC nanocapsule catalyst is highly beneficial for the gas transfer processes, and thus rapid gasification of carbon intermediates can be achieved. Another interesting multi-core@shell catalyst, Layered Double Hydroxide@SiO_2, was fabricated by coating a silica layer over Ni-Mg-Al LDH nanoplates[39]. It exhibited 30% CH_4 and 40% CO_2 conversion under 600 °C, 545,000 $mLg_{cat}^{-1}h^{-1}$ for 16 hours. It showed that the thickness of the silica shell significantly influenced the catalytic activity of LDH@SiO_2 multi-core@shell catalysts and concluded that when the silica shell was too thick, the diffusion resistance of reactants was too large and detrimental to the catalytic activity. Alternatively, embedding Ni nanoparticles into the hollow silicate-1 zeolite (Ni@S-1) was reported by a controlled strategy of the 'dissolution-recrystallization' process by hydrothermal treatment with tetrapropylammonium hydroxide (TPAOH) using impregnated Ni/S-1 zeolites [40]. Briefly, Ni

heteroatoms were incorporated into the S-1 lattice to form -Ni-O-Si-bonding during the recrystallization process, and TPAOH partially dissolve the S-1 zeolites during hydrothermal treatment to form a hollow structure, which linked NiO nanoparticles with S-1 zeolite and made NiO nanoparticles embed into the shell of S-1 zeolite upon calcination. It showed high activity and stability under 800 °C, a high WHSV of 100,000 $mLg_{cat}^{-1}h^{-1}$ for 150 hours, attributed to Ni nanoparticles being confined into the matrix of S-1 zeolite that resist sintering. However, most reported works did not thoroughly investigate the diffusion capabilities of the hierarchical nanostructures. The benchmarking of the catalytic activity has yet to be established, thus hindering the industrial exploitation. It is noted that core-shell or yolk-shell nano-framework would add another mass transfer barrier due to the shell diffusion effect, making the contact of reactants with active metals difficult[41]. Generally, kinetic analysis was carried out under extremely high space velocity[37,42]. The traditional diffusions from large granule stacking were already excluded from experimental and theoretical results. Then, one can infer the effects of diffusion on the reaction rates from the micro-nano perspective. One notable work proposed the shell diffusion effect by using a modified Weisz-Prater model to estimate the internal diffusion among the catalysts and simulate the mass transport over the individual nanocapsule-structured nanoreactors[43]. The model proposed that a "gas wall/hard blocker" formed on the openings of the shell pores causes interruption of the shell mass transfer and de-functionalizes the nanoreactor catalysts.

Herein, we report a $Ni@SiO_2$ nanocapsule catalyst (NSNC) as the bare core-shell catalyst for benchmarking for the dry reforming of methane. The catalyst's performance was significantly enhanced by employing mesoporous $Ni@SiO_2$ nanocapsule catalysts (M-NSNC). These mesoporous catalysts were obtained through a selective etching strategy, utilizing nickel-hydrazine@SiO_2 nanocapsules as precursors for modifying the NSNC. Also, the diffusion and intrinsic kinetic capabilities of the NSNC and M-NSNC were thoroughly investigated in order to establish the importance of the porosity in SiO_2 shell for dry reforming of methane.

2. Experimental

2.1. Material synthesis

$Ni@SiO_2$ nanocapsule (NSNC) catalyst. Prior to the synthesis of NSNC, nickel-hydrazine@SiO_2 nanocapsule was synthesized using the reverse microemulsion method adapted from the work of Gao et al.[44] with modifications. Briefly, 20 mmol of Brij O10 (Sigma-Aldrich), 2.4 mL of 0.67 M $NiCl_2$, and 60 mL of cyclohexane were stirred in a 250 mL round bottom flask for 15 minutes at 50 °C. Subsequently, 2 mL of hydrazine solution (50%) was added dropwise and reacted for 45 minutes. Subsequently, 20 mmol of diethylamine and 13.5 mmol of tetraethyl orthosilicate (TEOS) were added for the silica coating and proceeded for 5 hours, followed by centrifugation and washing with isopropanol. The collected slurry was redispersed in 80 mL of H_2O for 3 minutes in a 250 mL round bottom flask at room temperature. Then, 2 mL of ice-cold 4 M $NaBH_4$ was added dropwise, and bubbles were generated under stirring. The mixture was further reacted for another 2 hours to completely reduce the Ni-hydrazine complex to Ni metal (from pink to black color). Subsequently, the mixture was collected, washed several times with water and ethanol, and dried at 80 °C for 12 hours. Finally, the dried powder was subjected to thermal treatment of 650 °C (1.5 °$Cmin^{-1}$) for 6 hours in a muffle furnace.

Mesoporous $Ni@SiO_2$ nanocapsule catalysts (M-NSNCs). Prior to the synthesis of M-NSNCs, nickel-hydrazine@SiO_2 nanocapsule was synthesized using the reverse microemulsion method adapted from the work of Gao et al.[44] with modifications. Briefly, 20 mmol of Brij O10 (Sigma-Aldrich), 2.4 mL of 0.67 M $NiCl_2$, and 60 mL of cyclohexane were stirred in a 250 mL round bottom flask for 15 minutes at 50 °C. Subsequently, 2 mL of hydrazine solution (50%) was added dropwise and

reacted for 45 minutes. Subsequently, 20 mmol of diethylamine and 27 mmol of tetraethyl orthosilicate (TEOS) were added for the silica coating and proceeded for 5 hours, followed by centrifugation and washing with isopropanol. After drying the nickel-hydrazine@SiO$_2$ nanocapsule powder at 80 °C for 12 hours, 500 mg of the dried powder and 50 mL of 12.5 mM hexadecyltrimethylammonium bromide (CTAB) concentration were mixed (redispersed with an ultrasound bath for 2–3 minutes) in a round bottom flask under stirring at 50 °C for 3 minutes. The selective etching was achieved by adding 10 mmol of Na$_2$CO$_3$ into the mixture and reacting for 8 hours. Subsequently, the mixture was collected, washed several times with water and ethanol, and dried at 80 °C for 12 hours. Finally, the dried powder was subjected to thermal treatment at 650 °C (1.5 °Cmin^{-1}) for 6 hours in a muffle furnace. The corresponding samples were denoted as M-NSNC-1, M-NSNC-2, M-NSNC-3, and M-NSNC-4 for the incremental usage of CTAB with different concentrations of 12.5 mM, 25.0 mM, 50.0 mM, and 100.0 mM, respectively. A schematic illustration of the synthesis is depicted in Schematic 1.

2.2. Characterizations

The crystalline phase of the catalysts was characterized by the X-ray diffraction technique, using D8 Rikagu 9000 in the 2θ range of 10–80° under Cu Kα radiation. The specific surface area, total pore volume, and pore size distribution were measured by Micromeritics ASAP 2460 with pure N$_2$ physisorption at −196 °C. Before testing, the catalysts were degassed at 300 °C for 8 hours under vacuum. An inductively coupled plasma-mass spectrometry (ICP-MS), Agilent 720ES, was used to calculate each of the catalyst Ni wt% loadings, and the catalyst samples were digested with acid and diluted using 100 mL of deionized water before feeding into the instrument. The structural and Ni particle size were obtained from JEM 2100 transmission electron microscopy operated at 200 kV. The spectra of the surface chemical composition of the catalysts (XPS) were obtained using a Shimadzu Axis Ultra DLD spectrometer operated at 12 kV, 6 mA under the monochromatized Al Kα X-ray radiation source, and the chamber was maintained at a constant ultrahigh vacuum of 10^{-7} Pa. All spectra obtained were calibrated to correspond to C 1 s of 284.8 eV due to the charging effects. The temperature-programmed reduction of the catalysts was conducted to obtain the reduction profiles of Ni via the Micromeritics AutoChem II 2920. Typically, 30 mg of the sample was degassed under Ar gas at 300

°C for 30 minutes to remove the adsorbed impurities and moisture. Then, the gas flow switched to 10% H$_2$/Ar when it cooled to 50 °C for 30 minutes, and the sample was subjected to a temperature ramp of 10 °Cmin^{-1} to 900 °C. The H$_2$ consumption was monitored by an in-built thermal conductivity detector (TCD). The weight loss of the spent catalysts was analyzed using the STA 449F3 (NETZSCH) instrument in the temperature range of 25–1000 °C at a heating rate of 10 °Cmin^{-1}. The spent catalyst was also tested with a WITec Alpha 300 R Raman spectrometer equipped with a CCD detector. The laser has a wavelength of 532 nm and a power of 0.3 mW. Lastly, FTIR spectra characterization of the spent catalysts was conducted with a Perkin Elmer Spectrum Two FTIR spectrometer in order to establish the surface functional groups of the deposited carbon.

2.3. Catalytic performance test

The catalytic performance of the NSNC and M-NSNCs catalysts was carried out in a quartz tube fixed bed reactor with an inner diameter of 10 mm. 25 mg of the prepared catalyst (sieve with 200 mesh steel wire) was evenly mixed with zirconia beads (particle size of 0.4–0.5 mm) and filled up in the center of the quartz tube fixed bed reactor with a length of 3 cm followed by a reduction in 10%H$_2$/N$_2$ flow (30 mLmin^{-1}) at 750 °C for 3 hours. Next, a stoichiometric mixture of N$_2$:CH$_4$:CO$_2$ = 1:1:1 (weight hourly space velocity, WHSV of 144,000 mLg$_{cath}^{-1}$h^{-1}) was passed through the quartz tube fixed bed reactor loaded with catalyst, and the catalytic performance was tested individually at 800 °C. The effluent products were analyzed with an on-line gas chromatography (Fuli 9790) equipped with a 3-meter TDX-01 column and a thermal conductivity detector (TCD), and a desiccant was placed before the gas chromatography to scrub away any moisture in the effluent gases.

CH$_4$ and CO$_2$ conversions were determined using Eq. 1 and Eq. 2. The H$_2$/CO ratio was calculated according to Eq. 3 from the effluent gas, and the turnover frequencies of methane were computed according to Eq. 4 [45].

$$X_{CH_4}(\%) = \frac{(F_{CH_4,in} - F_{CH_4,out})}{F_{CH_4,in}} \times 100 \tag{1}$$

$$X_{CO_2}(\%) = \frac{(F_{CO_2,in} - F_{CO_2,out})}{F_{CO_2,in}} \times 100 \tag{2}$$
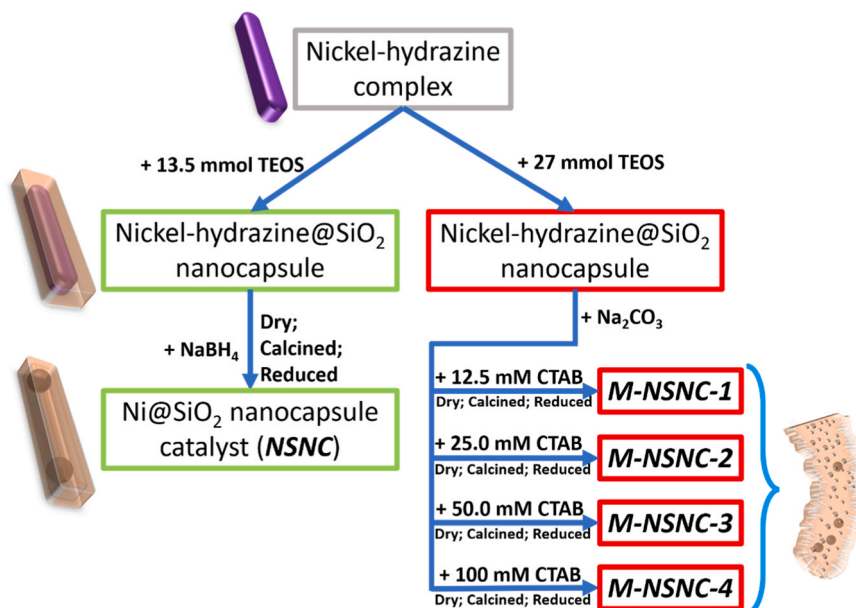
Schematic 1. Synthesis flow chart of the synthesis of NSNC and M-NSNCs catalysts.

$$H_2/CO = \frac{F_{H_2,out}}{F_{CO,out}} \qquad (3)$$

$$TOF_{CH_4} = \frac{r_{CH_4} \bullet M_{Ni}}{f_{Ni} \bullet D} \qquad (4)$$

Where $F_{CH_4,in}$, $F_{CH_4,out}$, $F_{CO_2,in}$, $F_{CO_2,out}$, $F_{H_2,out}$, and $F_{CO,out}$ are the inlet and outlet flow of respective reactant and product gases. r_{CH_4} is the CH_4 conversion rate, M_{Ni} is the molecular weight of Ni (58.69 gmol^{-1}), f_{Ni} is

the Ni weight fraction of the catalysts, and D = 97/d$_{TEM}$ (nm) is the estimated Ni dispersion[46].

2.4. Diffusion/kinetic test

Prior to the diffusion/kinetic test, the following conditions were fulfilled[47] as follow:
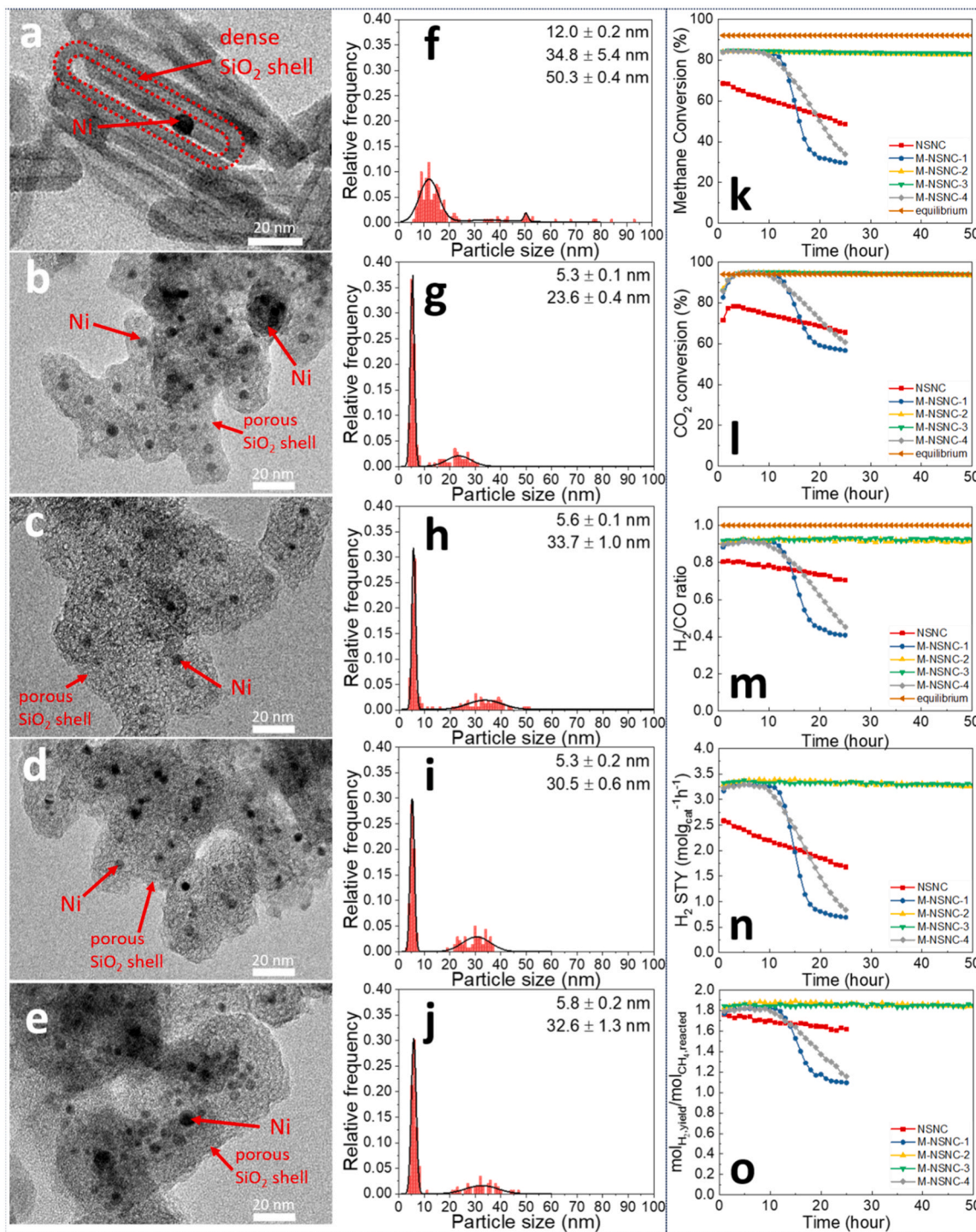
Fig. 1. TEM images of reduced NSNC (a), M-NSNC-1 (b), M-NSNC-2 (c), M-NSNC-3 (d), M-NSNC-4 (e). The scale bar is 20 nm, and the next column is their respective Ni nanoparticle sizes distribution (f-j). Catalytic performance of the catalysts in CH_4 conversion (k), CO_2 conversion (l), H_2/CO ratio (m), H_2 space-time yield (n), and H_2 yield per mole of CH_4 reacted (o) under WHSV of 144,000 mLgcat^{-1}h^{-1}, N_2:CH_4:CO_2 = 1:1:1 at 800 °C.

- The reactor diameter (D) must be at least 10 catalyst particle diameters (d_p) ($D/d_p > 10$); and
- For gas-solid systems, the catalyst bed length to catalyst particle diameter should be at least 50 ($L/d_p > 50$).

A reduction in catalyst particle size produces high-pressure drops. In this case, it can be resolved by mixing the fine catalyst particles with suitable inert particle sizes to guarantee a good fluid distribution and a low-pressure drop[48]. The catalysts were sieved below 100 μm for lab purposes to exclude the internal diffusion limitation, and a 200 mesh steel sieve was used in this work. The criteria of external diffusion limitation also have to be excluded; as such, the conversion rate has to be similar at any given flow rate with a fixed weight hourly space velocity, and the results are shown in Figure S1. In order to fulfill the criteria, a 60 mL min^{-1} flow rate (fixed WHSV of 1800,000 mLg$_{cat}^{-1}$h^{-1}) was used in this work.

2.4.1. Mass transport evaluation

The catalyst weight and feed flow were varied in the fixed-bed reactor to investigate the mass transfer limitation for the catalysts[47, 49]. Generally, the conversion of methane against the contact time (W/F, g$_{cat}$min cm^{-3}) was plotted with respective catalyst loading or feed flow in the fixed-bed reactor. Typically when approaching a lower contact time, the conversion of methane has a lower methane conversion. It was also a criterion to minimize the external resistance to mass transfer before evaluating the apparent CH$_4$ activation energy (Arrhenius plot) of the catalysts[47].

2.4.2. Kinetic evaluation

Once the diffusion evaluation was within the kinetic regime conditions, the catalyst was subjected to a stepped increase in temperature from 650 °C to 800 °C for the Arrhenius plot to get the apparent CH$_4$ activation energy. Generally, most reported works evaluated under ultrahigh space velocity[37,50,51] or below 20% methane conversion operated at lower temperatures [52,53] to reach kinetic regime conditions, but highly recommended to follow the criteria mentioned previously.

3. Results

3.1. Structure, catalytic performance, and physicochemical properties of NSNC and M-NSNC catalysts

The TEM images of the reduced NSNC and M-NSNC catalysts are shown in Fig. 1. It shows that the reduced NSNC catalyst has 3 variations of Ni nanoparticle sizes consisting of 12.0 ± 0.2 nm, 34.8 ± 5.4 nm, and 50.3 ± 0.4 nm. Meanwhile, the Ni nanoparticle size of M-NSNC catalysts has 2 variations ranging from 5.3 to 5.8 nm (up to 60% occupancy, Tables 1) and 23.6–32.6 nm due to different CTAB concentrations usage during synthesis. The larger Ni nanoparticle size in the catalysts could be due to the imperfection structure of the nickel-hydrazine@SiO$_2$ nanocapsule. A few "snaps" nickel-hydrazine@SiO$_2$ nanocapsule observable in Fig. 2a could lead to the larger Ni nanoparticle size when proceeding to the selective etching process. Following thermal treatment and

reduction, the SiO$_2$ nanocapsule fractures, enabling unhindered movement and growth of Ni nanoparticles within the NSNC catalyst, as depicted in Fig. 2b. Fortunately, the M-NSNC catalysts have a relatively small Ni nanoparticle size compared to NSNC due to the selective etching process with CTAB. Also, the XRD of the reduced NSNC and M-NSNC catalysts in Figure S2 suggest similar phenomena, with the NSNC catalyst having a distinct sharp peak at Ni(111) while the M-NSNC catalysts exhibited amorphous-like, indicating the relatively small Ni nanoparticles resemblance in the XRD signal. Theoretically, NSNC should have a 11.6 wt% of Ni loading in the composition of catalyst, and all modified (via selective etching) M-NSNCs catalyst with CTAB should have circa 5.8 wt% of Ni loading. However, ICP-MS analysis showed that, M-NSNC-1 has a much higher Ni wt% (7.70) than other catalysts and this could be due to a less amount of CTA$^+$ being used which contributed to the re-deposition of soluble silicate species during selective etching[38,54]. Whereas, when CTAB concentration at 25 mM or more were used, which resulted in a near theoretical value of 5.8 Ni wt %.

The catalytic performance of NSNC and M-NSNC catalysts with different porosity was subjected to dry reforming of methane reaction under 800 °C, 144,000 mLg$_{cat}^{-1}$h^{-1}, as shown in Fig. 1k-o. Noticeably, M-NSNC-2 and M-NSNC-3 outperformed other catalysts within 50 hours of time-on-stream. They remained stable at CH$_4$ conversion of more than 80% (Fig. 1k) and near equilibrium conversion of CO$_2$ (Fig. 1m). In contrast, the NSNC catalyst gradually deactivated from 68.5% to 48.5% of CH$_4$ conversion, while CO$_2$ conversion dropped from 78.4% to 65.5% within 25 hours. M-NSNC-1 and M-NSNC-4 catalysts have an initial high conversion of CH$_4$ and CO$_2$ within 10 hours but abruptly decrease in performance right after 10 hours of time-on-stream from 84.5% to 29.6% CH$_4$ conversion and 94.9–56.7% CO$_2$ conversion for M-NSNC-1 catalyst. Similar deactivation occurs in M-NSNC-4 catalysts from 84.3% to 33.8% CH$_4$ conversion and 94.7–60.8% CO$_2$ conversion. Fig. 1m shows the H$_2$/CO ratio of each catalyst and indicates that NSNC, M-NSNC-1, and M-NSNC-4 catalysts exhibited some extent of reverse water-gas shift reaction. Moreover, Fig. 1o shows the quantitative ratio of H$_2$ yield per mole of CH$_4$ reacted and ideally should approach a value of 2 mol$_{H2,yield}$/mol$_{CH4,reacted}$[55]. For instance, M-NSNC-2 and M-NSNC-3 catalysts continuously have a value above 1.8 mol$_{H2,yield}$/mol$_{CH4,reacted}$, showing that their low contribution in reverse water-gas shift reaction and remained stable throughout 50 hours of reaction. While NSNC, M-NSNC-1, and M-NSNC-4 showed severe occurrences of reverse water-gas shift reactions (less than 0.8 mol$_{H2,yield}$/mol$_{CH4,reacted}$ for NSNC; less than 0.5 mol$_{H2,yield}$/mol$_{CH4,reacted}$ for M-NSNC-1 and M-NSNC-4) that could damage the stability of the catalysts, as SiO$_2$ substrates are prone to hydrothermal instability[28,55,56]. It also reflected in the results of their low H$_2$ and CO space-time yield (Fig. 1n and S3). During the dry reforming of methane, a low H$_2$/CO ratio in the effluent signals a reverse water gas shift reaction, yielding water vapor. Another critical metric is the H$_2$ yield per mole of CH$_4$ reacted, ideally 2 moles. A low ratio indicates severe reverse water gas shift, as depicted in Fig. 1o. The water vapor from this reaction can negatively impact the SiO$_2$ substrate.

The N$_2$ adsorption-desorption isotherms of the NSNC and M-NSNC catalysts are shown in Fig. 3a. A Type-IV(b) isotherm with a high

**Table 1**
Properties of reduced NSNC and M-NSNC catalysts.

Sample	Ni loading (wt%)[a]	d_{TEM} (nm)[b]	Specific surface area (m^{2}g^{-1})	Total pore volume (cm^{3}g^{-1})	t-plot micropore volume (cm^{3}g^{-1})
NSNC	12.05	12.0 (81.8), 34.8 (14.7), 50.3 (3.5)	88	0.73	N/A
M-NSNC-1	7.70	5.3 (74.9), 23.6 (25.1)	526	0.49	0.21
M-NSNC-2	5.68	5.6 (66.1), 33.7 (33.9)	916	0.63	0.40
M-NSNC-3	6.06	5.3 (61.0), 30.5 (39.0)	941	0.74	0.38
M-NSNC-4	5.53	5.8 (73.4), 32.6 (26.6)	877	0.74	0.40

[a] Determined from ICP-MS.

[b] d_{TEM} is the nanoparticle size measured from TEM images in Fig. 1. *The parentheses referring to their respective percentage occurrence of different Ni nanoparticle size.*
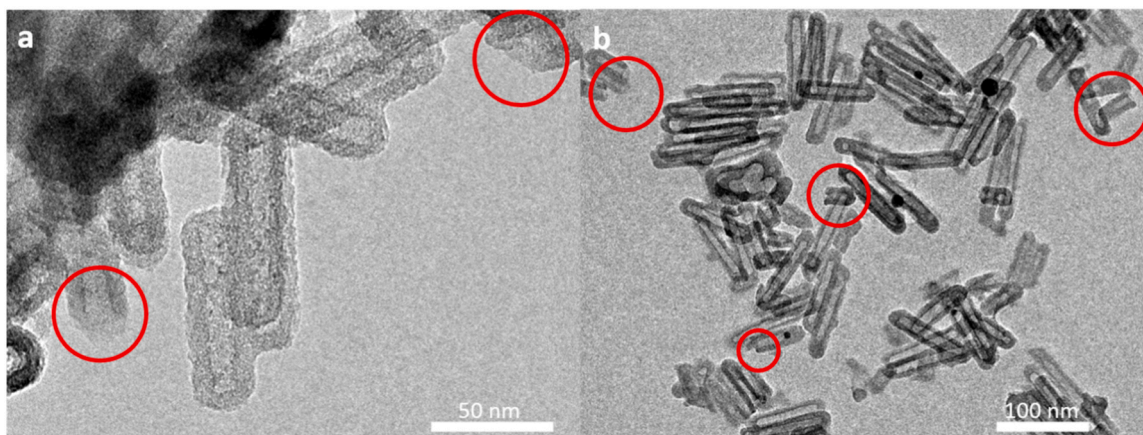
Fig. 2. TEM images of nickel-hydrazine@SiO$_2$ nanocapsule (a) and reduced Ni@SiO$_2$ nanocapsule catalyst, NSNC (b). Red circle indicated the imperfection structure of the nanocapsule.
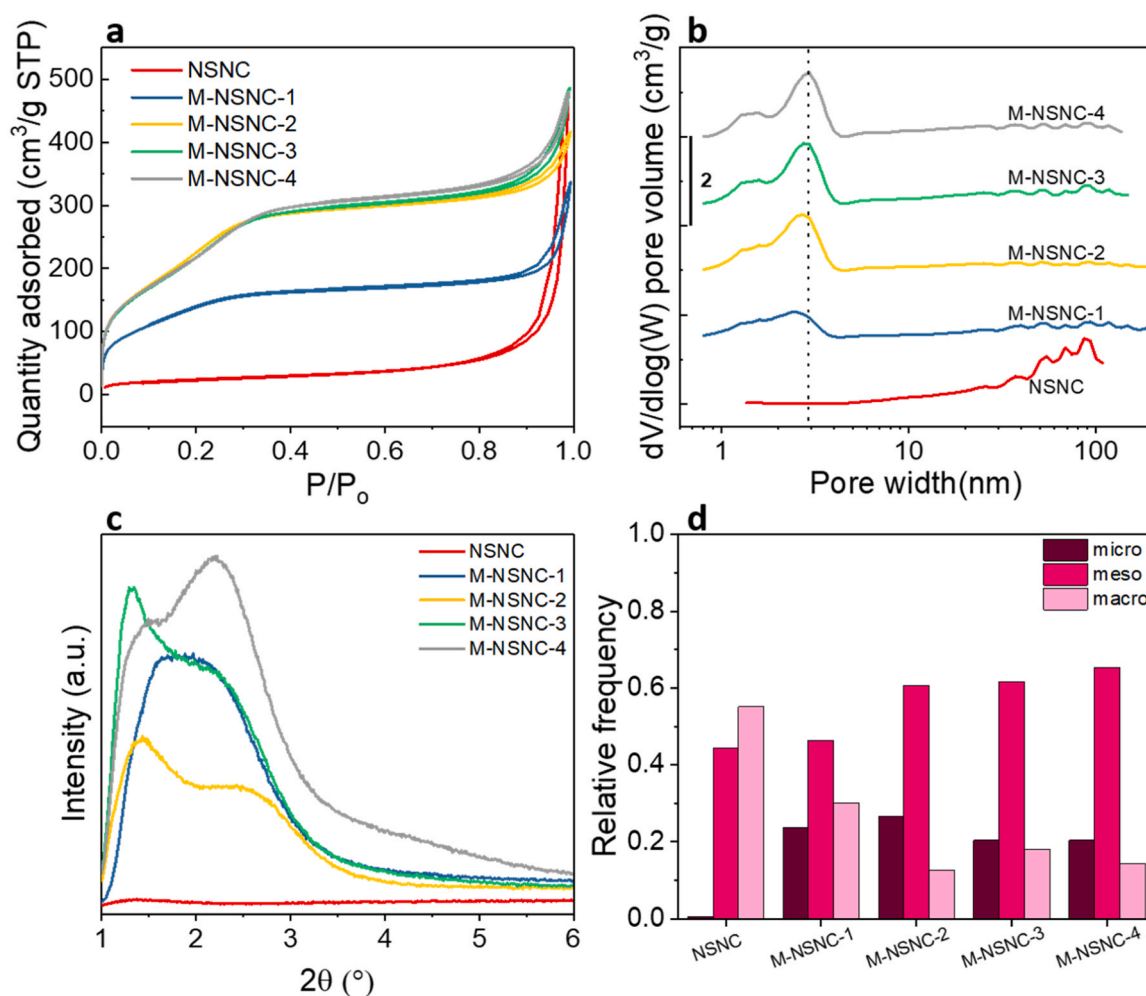
Fig. 3. The N$_2$ adsorption-desorption isotherm (a), pore size distribution (b), small-angle XRD (c), and relative frequency of micro-, meso-, and macropores (d) of the reduced NSNC and M-NSNC catalysts.

quantity of N$_2$ adsorption at lower P/P$_o$ was observed for M-NSNC catalysts, with M-NSNC-3 having the highest surface area of 941 m^{2}g^{-1} (Table 1), suggesting the catalysts are having mesopores of smaller width (< 4 nm), or cylindrical mesopores closed at the tapered end[57]. In contrast, the NSNC catalyst exhibits a Type-II isotherm with a low quantity of N$_2$ adsorbed (88 m^{2}g^{-1}, Table 1), suggesting the catalyst is

macroporous. All catalysts exhibited a Type H3 hysteresis loop with capillary condensation of between 0.8 < P/P$_o$ < 0.99, which is a non-rigid aggregate of plate-like particles and below P/P$_o$ of 0.8 could consider most pores exist as slit-shaped or close-end. The results of their pore size distribution in Fig. 3b suggest that increasing the CTAB concentration increases the amount of micropores (< 2 nm) and mesopores

(between 2 and 50 nm) in the catalysts and simultaneously enlarging the pore size from 2.3 to 2.9 nm. It also can be observed that the amount of macropores was diminished after the selective etching process with CTAB. Fig. 3c shows the low-angle XRD for all catalysts and the lattice of the pores has been expanded (low-angle shift in 2θ) with increasing usage of CTAB that has a good agreement with the pore size distribution. Whereas NSNC catalyst dominantly has a pore size distribution higher than 50 nm due to the inner long tubular shape of SiO$_2$. The relative percentage of different pores in each catalyst is shown in Fig. 3d to demonstrate the evolution of different pores due to the increasing usage of CTAB concentration. M-NSNC-2 has the highest percentage of micropores and the lowest percentage of macropores in the catalyst.

The Ni species in the NSNC and M-NSNC catalysts were characterized by H$_2$-TPR. The H$_2$-TPR assessed the reducibility of the Ni in the catalysts as shown in Fig. 4. It has been described that the reduction of Ni species in the catalysts could be categorized into three different types of α (bulk Ni, < 450 °C), β (450 °C ≤ β ≤ 800 °C), and γ (> 800 °C)[58]. The NSNC catalyst exhibits a prominent reduction peak at 597 °C, accompanied by a minor shoulder peak at 470 °C. Upon undergoing selective etching with CTAB, a hybrid of Ni species is formed in M-NSNC catalysts. M-NSNC-1 catalysts in Fig. 4 display a more robust reduction peak at 660 °C, extending across the α and β regimes, with a moderate shoulder peak at 422 °C. This shoulder peak might be attributed to the presence of bulk and/or weak interactions between Ni and SiO$_2$, while the main peak results from a strong metal-support interaction[59]. In contrast, M-NSNC-2 catalyst exhibiting a distinct reduction profile as compared to other catalysts, featuring a broad peak at 614 °C spanning all three Ni species, and a moderate peak at 926 °C, indicative of a stronger metal-support interaction. M-NSNC-3 catalyst has a major peak at 488 °C across the α and β regimes, accompanied by a moderate shoulder peak at 653 °C and another moderate peak at 974 °C. M-NSNC-4 catalyst reveals a significant peak at 702 °C spanning the β and γ regimes, with a moderate shoulder peak at 854 °C. A study revealed that a 3-D pore structure with a higher surface area would enhance the reduction temperature as compared to a 2-D pore structure with the equivalent Ni content[60]. This finding suggests the improved mass transfer properties in the 3-D pore structure catalyst for the dry reforming of methane. Additionally, another study on Ni/HAP demonstrated that by varying the synthesis temperature has led to different surface area and pore sizes, which impacting the size of Ni particles[61]. Specifically, a low-temperature (e.g. 20 °C) synthesis has resulted in a weakly bound NiO, leading to larger Ni particles, while fine particles with strongly bound NiO were observed in H$_2$-TPR between 300 and 450 °C. Many reported works indicated that having a hybrid of Ni species could promote the activities and stability of the catalysts in the dry reforming of methane[20,24,34,41,62]. The H$_2$-TPR results indicated that a suitable concentration of CTAB for the selective etching strategy would promote the reducibility of Ni species without jeopardizing the stability of the

catalyst that could be influenced by the pore characteristics in the SiO$_2$ nanocapsule shell. At the same time, a low or saturated concentration of CTAB could be adverse for the catalyst, such as difficulty to reduce all the Ni species to contribute for the active sites.

3.2. Evaluation of spent catalysts to establish the extend of carbon deposition

Carbon deposition or coking is inevitably one of the major causes of the deactivation of the catalysts during the dry reforming of methane that is caused by the methane dissociation and the Boudouard reaction. The thermogravimetric analysis determined the amount of carbon deposited in the spent catalysts (Fig. 5a). The early major weight loss was observed for all spent M-NSNC catalysts between room temperature and 200 °C, owing to the evaporation of the adsorbed moistures[63] (Fig. 5a and Figure S4). Bands associated with water were observed in two regions in FTIR (Fig. 5d and Figure S5) for the spent M-NSNC catalysts, H-O-H bending vibration at 1636 cm^{-1} and a group of bands of 3000–3800 cm^{-1}, corresponding to symmetric and asymmetric O-H stretching vibrations[64]. The increased in weight from 500 °C to 600 °C in TGA for all catalysts was due to metal Ni oxidizing to NiO[65]. Additionally, the weight increase above 800 °C could be caused by the solid-state reactions between the Ni and SiO$_2$[66]. The form of carbons on active metal surfaces generated during the dry reforming of methane were amorphous carbon or carbonaceous species predominantly in the lower temperature range of 200–500 °C and carbon nanotubes or graphitic carbon above 600 °C[67,68]. By taking their local minimum weight loss in their respective temperature region in Fig. 5a, Table 2 shows the carbon deposition rate of each spent catalyst, with M-NSNC-2 and M-NSNC-3 catalysts having the highest carbon being deposited. For instance, the spent NSNC catalyst exhibits a local minimum at 356 °C, contributing to a 0.09% reduction in amorphous carbon weight. The M-NSNC-1 catalyst displays local minima at 361 °C and 662 °C, resulting in 0.05% and 0.5% reductions in amorphous carbon and carbon nanotube weights, respectively. In the case of the spent M-NSNC-2 catalyst, local minima occur at 452 °C and 653 °C, leading to 2.2% and 0.1% reductions in amorphous carbon and carbon nanotube weights, respectively. Similarly, M-NSNC-3 exhibits comparable weight losses, registering 2.1% and 0.3% at 470 °C and 777 °C, respectively. Lastly, M-NSNC-4 demonstrates local minima at 360 °C and 728 °C, with corresponding weight losses of 0.15% and 0.3%. Fortunately, the weight loss that occurred in the spent M-NSNC-2 and M-NSNC-3 catalysts is predominantly amorphous carbon. Although the spent NSNC catalyst exhibits no weight loss in TGA, the XRD spectra in Fig. 5b shows that the spent NSNC has a strong graphite signal at 2θ = 26.5°. It demonstrates that the NSNC catalyst experienced severe carbon deposition.

A thorough carbon deposition characterization was essential due to the challenging detection of carbon by TGA and XRD. Understanding the specific type of the deposited carbon leading to the catalyst deactivation/poisoning is of particular interest. Further validation with Raman characterization of the spent catalysts is shown in Fig. 5c. It shows all the catalysts have two-band peaks at 1345 cm^{-1} and 1571 cm^{-1}, identified as the amorphous and sp2 carbon[69], with NSNC having the intensive G band among them. One can determine their crystallinity/disordered nature of the deposited carbon after the dry reforming of methane. If the ratio of I_D/I_G is lower than 1, it indicates that high graphitization of carbon has occurred in the catalyst and vice versa. Also, the peak at 2679 cm^{-1} indicating the characteristic of carbon nanotubes[70], and the spent NSNC catalyst has the most prominent signals among them. Thus, the spent NSNC has an I_D/I_G ratio of 0.75, indicating severe coking despite no weight loss from TGA. In contrast, M-NSNC-1, M-NSNC-2, M-NSNC-3, and M-NSNC-4 catalysts have the I_D/I_G ratio of 2.00, 1.50, 1.67, and 1.38, respectively, signifying the carbon deposited mostly were amorphous compared to NSNC catalyst. FTIR was also conducted to crosscheck the possible surface functional group of the spent catalysts. It could detect the occurrence of carbon with possible assignments for
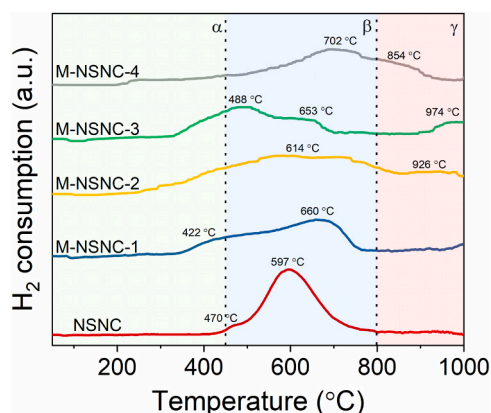

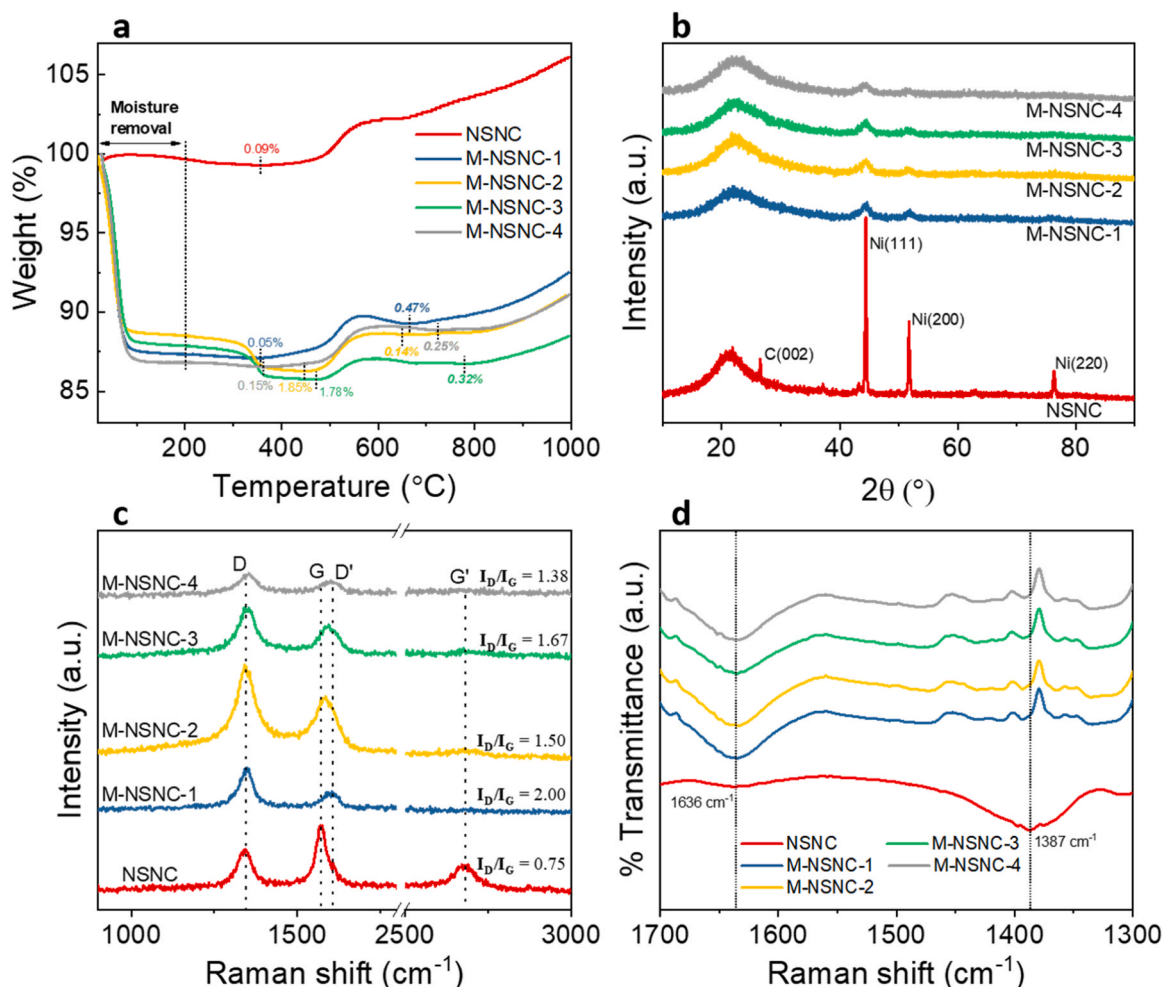**Fig. 4.** H$_2$-TPR of calcined NSNC and M-NSNC catalysts.

Fig. 5. TGA (a), XRD (b), Raman (c), and FTIR (d) spectra of spent NSNC and M-NSNC catalysts.

Table 2

The Ni particle size, carbon deposition rate, and I_D/I_G ratio of spent NSNC and M-NSNC catalysts.

Sample	$d_{TEM,spent}$ (nm)[a]	Carbon deposition rate ($\mu g_C g_{cat}^{-1} h^{-1}$) at low T[b]	Carbon deposition rate ($\mu g_C g_{cat}^{-1} h^{-1}$) at high T[c]	I_D/I_G ratio
NSNC	16.7 (28.4), 23.0 (9.1), 26.2 (32.7), 50.9 (29.8)	36	N/A	0.75
M-NSNC-1	6.9 (11.1), 10.2 (39.3), 14.1 (29.3), 17.5 (18.5), 26.0 (1.8)	16	192	2.00
M-NSNC-2	6.1 (48.9), 8.9 (11.4), 11.6 (30.9), 20.3 (8.8)	368	22	1.50
M-NSNC-3	8.1 (60.0), 11.9 (12.7), 15.2 (17.1), 25.6 (10.2)	356	64	1.67
M-NSNC-4	7.5 (41.2), 10.2 (9.3), 18.0 (18.9), 22.7 (5.6), 26.6 (13.8), 29.4 (11.2)	6	108	N/A

[a] Measured from TEM images in Figure S6.

[b] Weight loss taken at 300 °C to local minima before 500 °C from TGA (Fig. 5a).

[c] Weight loss taken at the local maxima and local minima between 500 °C to 900 °C from TGA (Fig. 5a).

carbon nanotube or graphite with its unique vibration mode in FTIR spectra[71]. Fig. 5d shows that NSNC has a major transmittance peak at 1387 cm^{-1} that could be assigned to the symmetrical bending of the alkyl group in carbon nanotubes. The observation shows NSNC has the signal of symmetrical bending of the alkyl group in carbon nanotubes. Both results from Raman and FTIR suggesting severe high crystallinity carbon nanotube deposited in the catalyst.

Fig. 6 shows the HRTEM of each spent catalyst. As anticipated, all the catalysts have carbon being deposited after the tests. NSNC has the most severe coking as the carbon deposited would encapsulate the active Ni metal (Fig. 6a). Upon closer inspection of the TEM images in Figure S6, it

is evident that the M-NSNCs catalyst would retain its porous Ni@SiO$_2$ nanocapsule structure after the test, except NSNC. Carbon nanotubes were also observed in the spent M-NSNC-1, M-NSNC-2, and M-NSNC-3 catalysts, whereas no apparent carbon nanotube presence in M-NSNC-4. An extensive characterization of the deposited carbon was conducted with XPS C 1 s (Fig. 6f) to comprehend the types of carbon being deposited in the spent catalysts. Metal carbides (283.0 eV), filament carbon (283.8 eV), graphitic carbon (284.6 eV), adventitious carbon (284.8 eV), C-O (285.7 eV), C=O (286.7 eV), and O-C=O (283.8 eV) present in the spent catalysts[32,72]. It showed that the spent M-NSNC-2 and M-NSNC-3 catalysts have less filamentous and graphitic
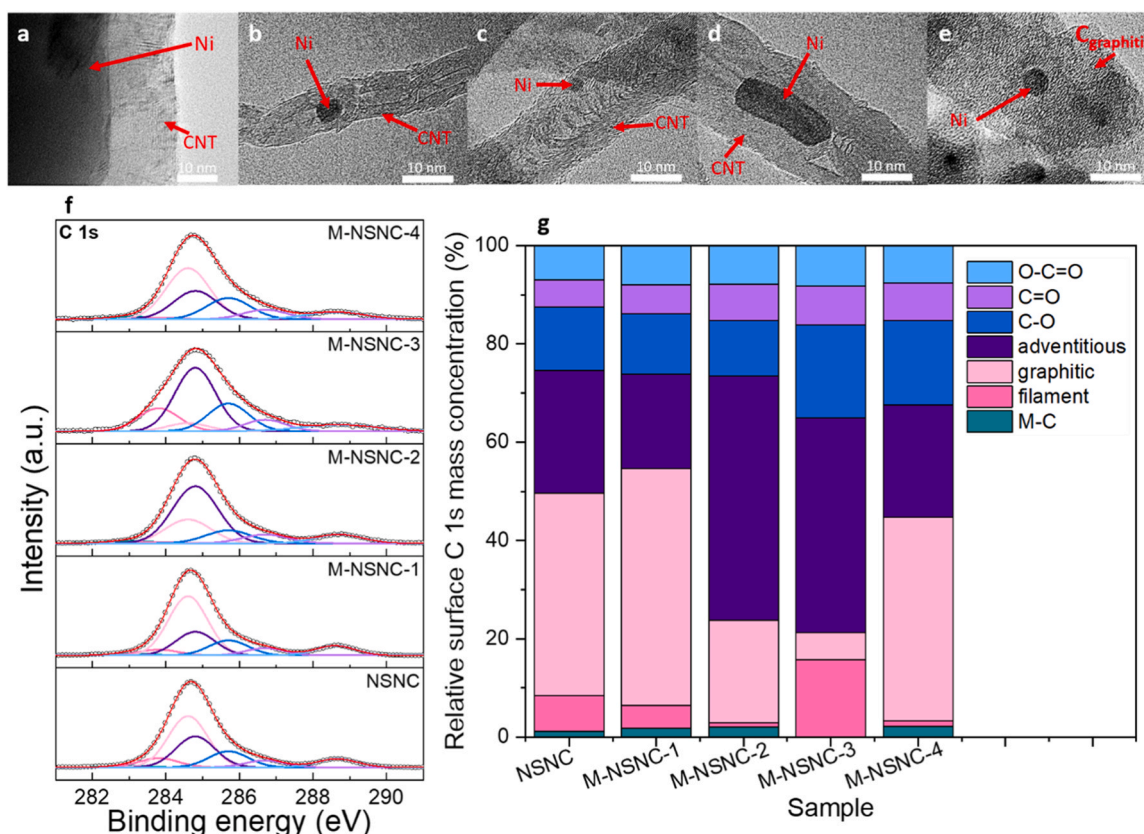
Fig. 6. TEM image of spent NSNC (a), M-NSNC-1 (b), M-NSNC-2 (c), M-NSNC-3 (d), and M-NSNC-4 (e) catalyst, XPS C 1 s spectra (f) and relative surface C 1 s mass concentration (g) of the spent catalysts.

carbon being deposited in the catalyst, with a relative amount of 23.8% and 21.3%, respectively. Taking graphitic, filamentous, and metal carbide as the significant coking in the spent catalysts (NSNC, M-NSNC-1, and M-NSNC-4), which have a relative amount of 49.7%, 54.7% and 44.7%, respectively. A tabulation of their fraction was presented in the Supplementary material, Table S2. A comprehensive viewpoint in their coking degree, M-NSNC-2 and M-NSNC-3 catalysts can resist the deposition of high crystallinity carbon. The results from TGA showed that M-NSNC-2 and M-NSNC-3 were primarily amorphous carbon, and XRD shows no graphite peak occurs. Also, Raman results suggested that the carbon deposited was disordered that could be easily eliminated. Though TEM shows that the spent M-NSNC-2 and M-NSNC-3 contained some carbon nanotubes, they did not disrupt the catalyst activity. The carbon nanotubes could be due to some of the imperfection structure of nickel-hydrazine@SiO$_2$ nanocapsule or fractured during synthesis that causes some large Ni nanoparticles, which are prone to produce carbon nanotubes in the dry reforming of methane[10]. Overall, it demonstrated an adequate usage of CTAB concentration able to resist higher-ordered carbon deposition for the dry reforming of methane for M-NSNC catalysts.

3.3. Evaluation of diffusivity between dense and porous SiO$_2$ nanocapsule catalysts

Before the diffusion and kinetic evaluation, several tests were conducted to ensure that the reactor operated in the kinetic conditions (excluding internal and external mass transfer resistance) and followed the instructions from Section 2.4. The NSNC and M-NSNC-2 catalysts were chosen for the diffusion evaluation by changing the contact time (W/F) in the reactor to emphasize the difference between a dense SiO$_2$ shell and a porous SiO$_2$ shell[73]. Fig. 7 shows the mass transfer tests for NSNC and M-NSNC-2 catalysts, indicating each diffusion capability.

NSNC catalysts would require prolonged contact times for a steady methane conversion (222.22 $\times 10^{-5}$ g$_{cat}$mincm^{-3}), while M-NSNC-2 catalysts achieved consistent conversion at a significantly shorter contact time (16.67 $\times 10^{-5}$ g$_{cat}$mincm^{-3}), *circa.* 13 times better than NSNC catalysts. From the classical 7 steps of a catalytic reaction[74], it can be depicted that the reaction pathway is more favorable in M-NSNC-2 due to much lower physical hindrance in the boundary layer and pore diffusion. A contact time of W/F = 3.33 $\times 10^{-5}$ g$_{cat}$mincm^{-3} (WHSV = 1800,000 mLg$_{cat}^{-1}$h^{-1}) was used (under kinetic regime) to evaluate the intrinsic kinetic of the catalysts from temperature range 650–800 °C, and the apparent CH$_4$ activation energy of the dry reforming of methane reaction was evaluated. The apparent activation energy of 209.0 and 67.9 kJ/mol was determined through the Arrhenius plot (Fig. 8a) for NSNC and M-NSNC-2 catalysts, respectively. It was reported that the experimental CH$_4$ dissociation activation energies of 52.7, 26.8, and 55.6 kJ/mol on Ni(111), Ni(100), and Ni(110), respectively, were measured by Auger electron spectroscopy[75]. However, most literatures reported varying values from 35 to 117 kJ/mol[76]. For instance, a reported Ni-SiO$_2$ catalyst has an apparent activation energy of 80.3 kJ/mol[49], Pt/ZrO$_2$ catalyst was reported to have 82.0 kJ/mol [77], and Ni-3La$_2$O$_3$/SiO$_2$ catalyst has 43.5 kJ/mol[78]. Their difference in the apparent activation energy depends on the nature of support, promoters, and preparation route. Similarly, to NSNC and M-NSNC-2 catalysts, the difference of a dense and a porous SiO$_2$ shell showed a huge gap on the apparent activation energy of CH$_4$ and is highly reflected in their difference in physical properties of the catalyst. Also, the TOF$_{CH4}$ of the catalysts shown in Fig. 8b indicates the difference in performance between the catalysts due to the usage of CTAB concentration.
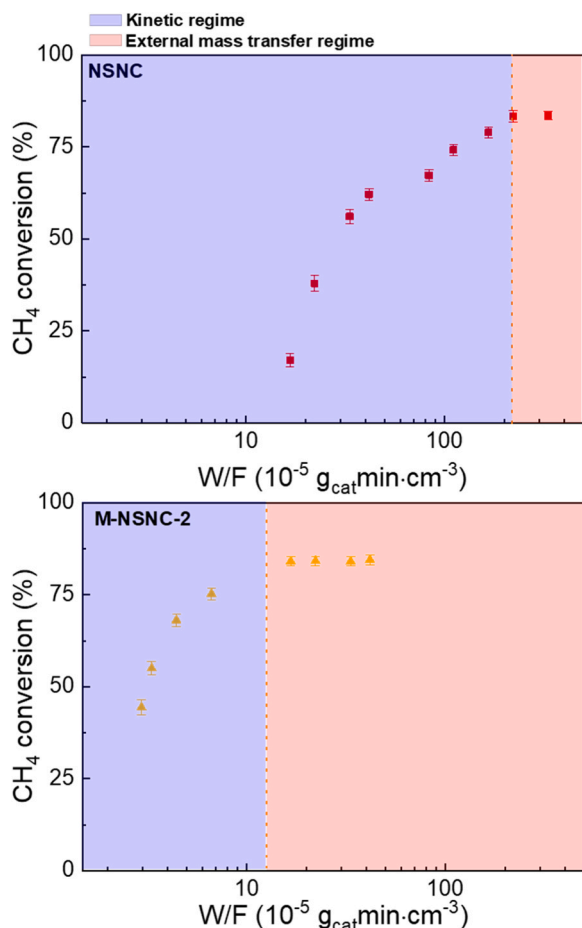
Fig. 7. Mass transfer tests for reduced NSNC and M-NSNC-2 catalysts under 800 °C with varying contact times, where F is the total flow rate (mLmin^{-1}), and W is the catalyst weight (g)[73].

4. Discussion

4.1. Synthesis of NSNC and M-NSNC catalysts

The Ni@SiO$_2$ nanocapsule particles were synthesized by a reverse microemulsion method adapted from Gao et al. with modification[44]. They have successfully demonstrated a gram-scale synthesis of nickel-hydrazine complex encapsulated in silica nanotubes. Meanwhile,

they could also obtain both nickel hydroxide nanorods after etching the SiO$_2$ shell with NaOH and silica nanotubes after etching the nickel-hydrazine complex with HCl. Similar reported works have also successfully synthesized Ni@SiO$_2$ nanocapsule with a different approach[79,80]. They suggested the tubular dimension was due to the decomposition of a portion of insoluble Ni(N$_2$H$_4$)$_3^{2+}$ complex with the extension of aging time in the presence of OH$^-$ (NH$_4$OH) to produce gaseous bubbles, which then leads to the elongation of the nanocapsule micelle by the gaseous product via buoyancy. It utilizes the OH$^-$ or existing reduced Ni as a catalyst to promote the decomposition of Ni(N$_2$H$_4$)$_3^{2+}$ complex by adding ammonia to improve the elongation and dispersion of micelles. Also, they demonstrated that the inner cavity length of Ni@SiO$_2$ nanocapsule was increased with the prolonged aging time during synthesis and was found to be an excellent catalyst for the dry reforming of methane attributed to its sufficient inner cavity space that can enhance the Ni nanoparticles dispersion and increase activity, which facilitates the gasification of intermediate carbon during reaction [37].

However, the synthesis mechanism in Gao et al. [44] works was different because the base it used was diethylamine (DEA) which would not deform or decompose the structure of the nickel-hydrazine complex and was stable throughout the SiO$_2$ coating. Also, their nickel hydroxide nanorod could be a good template for further coating with a functional SiO$_2$ shell. The difference and novelty we used here the selective etching method instead to further treat nickel-hydrazine@SiO$_2$ nanocapsule in a mild alkaline solution assisted with CTAB, simultaneously forming nickel hydroxide and selectively etching the dense SiO$_2$ into a porous SiO$_2$ shell. The synthesis route is visualized via TEM in Fig. 9 to show the evolution of the NSNC and M-NSNCs catalyst. The TEM image of nickel-hydrazine@SiO$_2$ has some particulate dots in the inner cavity of the SiO$_2$ nanocapsule was due to the high electron beam radiation during TEM imaging that caused the decomposition and recrystallization of the nickel-hydrazine complex[44]. When it was reduced by NaBH$_4$, obvious Ni nanoparticles were distributed randomly in the inner SiO$_2$ nanocapsule. Finally, it was subjected to thermal treatment, followed by a reduction to get the Ni@SiO$_2$ nanocapsule catalyst (NSNC) and would be the reference sample for this work. Unfortunately, most Ni nanoparticles were sintered or agglomerated after thermal treatment and reduction, and only a few were encapsulated inside the cavity. Contrary, the Ni dispersion in M-NSNC showed fine dispersion of Ni even after the thermal treatment and reduction, comparatively similar to snow peas [81] structures (*Pisum sativum* var. *saccharatum*) with pores, as shown in Fig. 9. The selective etching method was demonstrated in multiple works owing to the nature of the cationic surfactant of CTAB in alkaline solutions[38,54,82]. Three important steps are involved in converting solid SiO$_2$ into mesoporous structure: 1) adsorption of CTA$^+$ on the
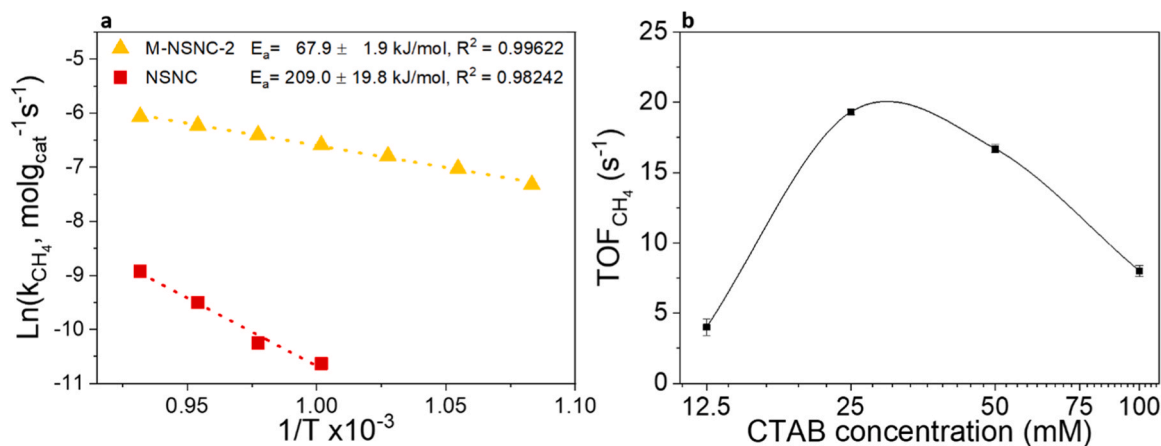

Fig. 8. Arrhenius plot (a) of NSNC and M-NSNC-2 catalysts under 1800,000 mL g$_{cat}^{-1}$h^{-1} and TOF$_{CH4}$ (b) of the catalysts with increasing usage of CTAB concentration under 144,000 mLg$_{cat}^{-1}$h^{-1}, 800 °C.
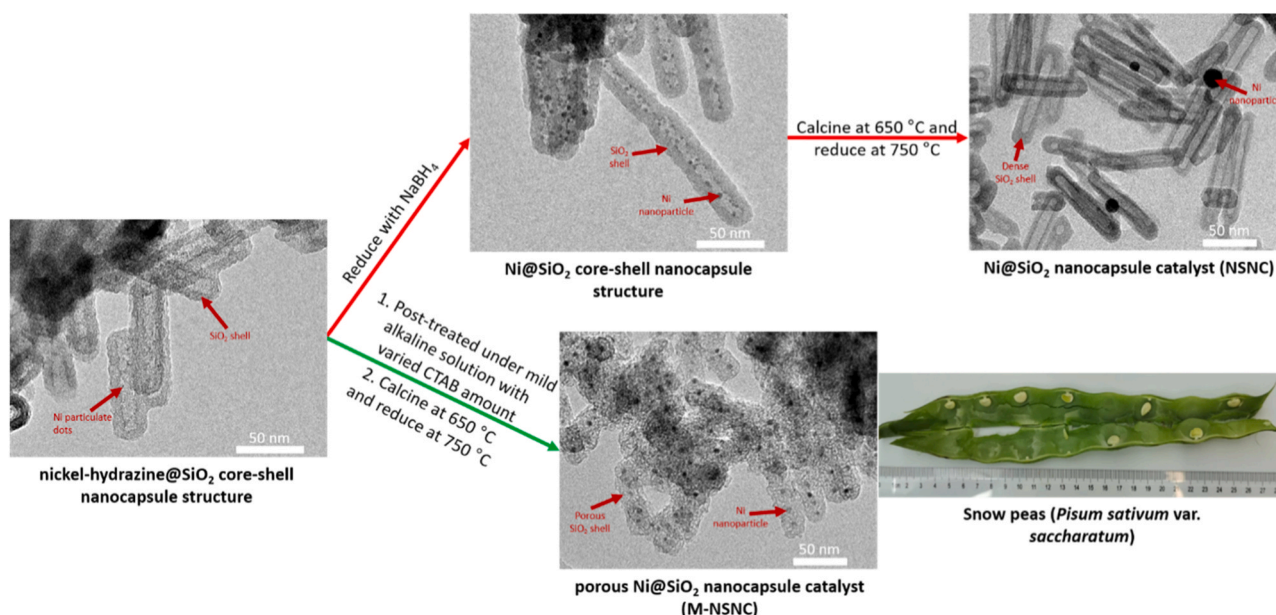
Fig. 9. The flowchart of the synthesized NSNC and M-NSNC catalysts.

surface of solid SiO_2; 2) dissolution of SiO_2 to form soluble silicate species; and 3) co-assembly of CTA^+ with some soluble silicate species to form mesoporous structure. By utilizing the mechanism, one can anticipate functionalizing a porous SiO_2 from a dense SiO_2 shell. The mechanism of CTAB was illustrated and explained in the Supporting Information.

4.2. Stability of the catalysts

The performance variation in the M-NSNC catalyst is evident due to the usage of CTAB concentration and we increased the concentration usage up to the theoretical saturation point[83] (0.1 M at 20±2 °C) as the parameter study to indicate the importance of porosity in the SiO_2 shell. As previously mentioned, CTAB acted as a template for the generation of the porous structure of the SiO_2 shell and this would be reflected in their difference in Ni nanoparticle size as characterized by TEM after the test (Figure S6). The spent M-NSNC-2 has the least sintered Ni nanoparticles from 5.6 to 6.1 nm (Fig. 1 and Figure S6), while other catalysts displayed a more severe Ni nanoparticle sintering. For example, the reduced M-NSNC-1 has a relatively high occurrence of 5.3 ± 0.1 nm Ni particle distribution, and after the test, showing poor Ni particle distribution (6.9–26.0 nm) as compared to the spent M-NSNC-2 and M-NSNC-3 catalysts. Similarly, the M-NSNC-4 catalyst had a poor Ni particle size distribution ranging from 7.5 to 29.4 nm after the test. The sintering of the Ni particles could be highly related to their difference in pore characteristics, especially the pore size distribution. Fig. 3b indicates that increasing CTAB concentration would gradually increase the pore size from the highest peaks of 2.3 nm to 2.9 nm, which could endorse the active metal migration through Ostwald ripening and particle coalescence[10]. Insufficient or excessive of CTAB concentration would lead to the sintering of Ni particles, causing particle size enlargement, whereas optimal CTAB concentration would hinder the Ni particle size growth, thus optimizing the catalyst for the dry reforming of methane. Validation using small-angle XRD (Fig. 3c) also suggested that the pores were expanded with the increased usage of CTAB concentration. Also, the poor Ni particle distribution in the spent M-NSNC-1 catalyst could be due to the relatively high amount of macropores (Fig. 3d) as compared to other catalysts that possibly accelerate the sintering of Ni particles. Since the M-NSNC-1 catalyst was synthesized from the nickel-hydrazine@SiO_2 nanocapsule, the macropores feature could be derived from the inner cavity of the nanocapsule that resulted

in a relatively high amount of macropores in M-NSNC-1 and the pore size distribution of NSNC also suggested a high occurrence of macropores (> 50 nm, Fig. 3b). The phenomena could be the low amount of adsorption of CTA^+ on the surface of solid SiO_2 in M-NSNC-1 during synthesis, which contributes less to microporous and mesoporous pores generation[84]. A study employing direct imaging techniques to investigate the migration of active metal nanoparticles within various mesoporous silica structures has been conducted[85]. The findings proposed that in order to mitigate Ostwald ripening and particle migration, catalysts should feature not only highly uniform active metal particle size but also an ample presence of pores on the supporting material in order to prevent the sintering of the active metal particles. Figure S6g shows that the Ni nanoparticles agglomerated in the inner cavity of M-NSNC-1 after the test. Thus, the M-NSNC-1 catalyst exhibited poor stability and loss activity after 10 hours of time-on-stream. The deactivation in the M-NSNC-4 catalyst similar to M-NSNC-1 catalyst. It appears that the Ni active metal sintered after the test (Figure S6), the Ni particle size distribution profile shifted to larger Ni particle size (from 5.8 nm, Table 1 to 7.5–29.4 nm, Table 2). In summary, low or excessive usage of CTAB resulted in poor stability for M-NSNC catalysts in the dry reforming of methane. In contrast, fair usage of CTAB concentration produces stable M-NSNC catalyst with characteristic of small and homogeneous dispersed Ni nanoparticles, high surface area, and hybrid of Ni species that contributed to the superior performance in the dry reforming of methane. The deactivation of the NSNC catalyst might be attributed to the traces of boron residue[86], which could have adverse effects on the nanostructure, especially at high temperatures. Additionally, the XPS survey in Figure S7 identified the presence of traces of boron in the reduced NSNC sample. A comparison of recent Ni-based catalysts for long-term stability tests for dry reforming of methane and this work have been summarized in Table S3.

4.3. Carbon resistivity between the catalysts

The spent NSNC and M-NSNC catalysts appeared to have carbon deposited in the catalysts after 50 hours time-on-stream. However, the carbon deposited differs from each other. For example, the spent NSNC catalyst showed no weight loss in TGA analysis (Fig. 5a) but has a prominent signal of carbon peak characterized by XRD (Fig. 5b). Also, Raman and FTIR (Figs. 5c and 5d) showed that the carbon deposited in the spent NSNC catalyst is mainly higher-ordered carbon, such as carbon

nanotubes or graphite. In contrast, other catalysts showed higher intensity of disordered carbon or carbonaceous group. Though TGA showed that the spent M-NSNC-2 and M-NSNC-3 catalysts had the highest weight loss, it can be considered that the carbon deposited is mainly amorphous (Table 2). Instead, the spent M-NSNC-1 catalyst has the highest weight loss in the temperature range at 500–900 °C with a carbon deposition rate of 192 $\mu g_C g_{cat}^{-1} h^{-1}$. Further validation from XPS C 1 s (Fig. 6f) of the spent catalysts showed that M-NSNC-2 and M-NSNC-3 catalysts could resist higher-ordered carbon deposits with the lowest relative amount of graphitic and filament carbon detected.

4.4. Diffusivity difference between NSNC and M-NSNC-2 catalysts

An important aspect for consideration is the diffusion capability of the catalyst. Applying classical mass transfer criteria would allow the characterization of the catalyst's minimum residence time for diverse catalytic applications. Recent advancements in synthesizing core-shell nanocapsules, particularly in nanomaterials, have provided a valuable model for conducting detailed diffusivity studies. In this context, NSNC was a type of core-shell nanocapsule catalyst with a dense SiO_2 shell that could "block" the transport processes during the dry reforming of methane and being used as the reference model. Fig. 7 shows the limit for the highest methane conversion in the NSNC catalyst which is approximately 222.22 $\times 10^{-5}$ $g_{cat} min cm^{-3}$, while the M-NSNC-2 catalyst shows a shorter contact time approximately at 16.67 $g_{cat} min cm^{-3}$. It indicates that the porosity in the M-NSNC-2 catalyst would promote the transport processes and less physical hindrance in the boundary layer and pore diffusion. M-NSNC-2 catalyst has a greater surface area (916 $m^2 g^{-1}$) than NSNC catalyst (88 $m^2 g^{-1}$), contributing to enhance transport processes due to their difference in surface area. The work of M. Arsalan Ashraf et al. found that increasing the surface area of the catalyst would decrease the diffusion limitation effect that could provide more transport processes and reactions in alumina monoliths[87]. A modelling study proposed by Wang et al. [43] indicated that a "gas wall/hard blocker" formed on the openings of the shell pores would cause interruption of the SiO_2 shell mass transfer and de-functionalize the nanoreactor catalysts. Also, Fig. 8a showed the apparent CH_4 activation energy of NSNC (209.0 kJ/mol) and M-NSNC-2 (67.9 kJ/mol) catalysts, indicating that the porous SiO_2 shell would promote the transport phenomena and enhances its performance. It suggested that the pore characteristics in the SiO_2 shell would play a significant role in the catalytic reactions.

The summary of recent core-shell catalysts from literature and M-NSNC catalysts are tabulated in Table 3. Nearly half of the reported works have yet to assess the core-shell catalysts' kinetic evaluation. The frequently cited WHSV value in publications lacks robust evidence to firmly establish its investigation within the kinetic regime. While a high WHSV suggests operation within the kinetic regime, most studies lack concrete evidence, such as a mass transfer test (e.g., Fig. 7) for the catalysts. Despite recent breakthroughs in nanomaterials for catalysis, clear procedures for evaluating the mass transfer capability limits of reported catalysts are still lacking. Taking classical mass transfer criteria to the extreme can unveil the full potential of recently developed nanocatalysts. Otherwise, there would be a risk of misinterpreting the

intrinsic kinetic activity of the M-NSNC-2 catalyst if it had been tested under the kinetic conditions of the NSNC catalyst. Thus, Fig. 10 illustrates the difference in diffusion capability of a dense SiO_2 shell and a porous SiO_2 shell that affects the overall performance of dry reforming of methane and justifies the intrinsic kinetic activity of the developed novel catalysts in order to summarize the importance of the context in this work.

5. Conclusions

The pursuit of superior catalysts for high-temperature dry reforming of methane has driven innovative research endeavours strive to enhance catalytic performance and tackle challenges associated to conventional core-shell catalyst designs. In this study, a pioneering approach is being introduced, involving the development of porous Ni@SiO_2 nanocapsule catalysts synthesized via selective etching in a mild alkaline solution with varying concentrations of CTAB. This method aims to overcome limitations associated with dense and inert oxide shells in conventional core-shell catalysts which tend to hinder intrinsic kinetics and gas diffusion. Moreover, our unique porous core-shell nanocapsule catalysts have demonstrated effectiveness in overcoming such limitations, whilst mitigating active metal sintering and coking. The optimized catalyst, M-NSNC-2 containing small Ni nanoparticles (5.3 nm) within a porous capsule displayed an exceptional high surface area exceeding 900 $m^2 g^{-1}$ with remarkable catalytic activity of a methane conversion rate exceeding 82%, stability over 50 hours, robust resistance to sintering, agglomeration, and higher-ordered carbon deposition. Such outstanding performance would warrant this porous nanocapsule catalyst as a highly promising candidate for high-temperature dry reforming of methane.

Furthermore, such innovative porous nanocapsule catalyst also offered unprecedented insights into diffusion capabilities, applying classical mass transfer criteria extensively to unveil the hidden potential of the developed nanocatalysts for the first time. The M-NSNC-2 catalyst exhibited especially superior performance, with nearly a 13-fold enhancement in mass transfer diffusivity as compared to conventional NSNC catalyst. This catalyst also exhibited an apparent CH_4 activation energy of 67.9 kJ/mol at a kinetic regime of 1800,000 mL $g_{cat}^{-1} h^{-1}$, emphasizing its efficacy in catalyzing dry reforming of methane. These findings can assist future strategies in designing novel catalysts, especially for high-temperature reaction.

CRediT authorship contribution statement

Zi-Yian Lim: Prepared, characterized, tested the developed catalysts and wrote the original draft. **Junling Tu:** Provided part of the chemical reagents and helpful discussion in N_2-isotherm patterns. **Fengling Zhou:** Offered the testing of N_2-isotherm and discussion about the pore size distribution. **Baiman Chen:** Offered a help for the assembly of the test rig. **Kwang Leong Choy:** Supervised the project, reviewed, and wrote the paper.

Declaration of Competing Interest

The authors declare that they have no known competing financial

Table 3
A summary of recently reported core-shell catalyst for kinetic evaluation from literature and this work.

Catalyst	WHSV (mLg$_{cat}^{-1}$h^{-1})	Gas composition	Temperature range (°C)	Apparent CH_4 activation energy (kJ/mol)	Ref.
Ni@SiO_2-1 h	600,000	N_2:CH_4:CO_2 = 4:3:3	550–700	51.6	[34]
In$_{0.5}$Ni@SiO_2	72,000	CH_4:CO_2 = 1:1	550–750	99.0	[35]
Ni-SiO_2@SiO_2	36,000	CH_4:CO_2 = 1.5:1	N.A.	N.A.	[36]
Ni@SNC-6 h	1440,000	CH_4:CO_2 = 1:1	650–800	53.2	[37]
LDH@SiO_2-thin	545,000	N_2:CH_4:CO_2 = 2:1:1	N.A.	N.A.	[39]
15%Ni@S-1	180,000	CH_4:CO_2 = 1:1	N.A.	N.A.	[40]
NSNC	1800,000	N_2:CH_4:CO_2 = 1:1:1	650–800	209.0	This work
M-NSNC-2	1800,000	N_2:CH_4:CO_2 = 1:1:1	650–800	67.9	This work
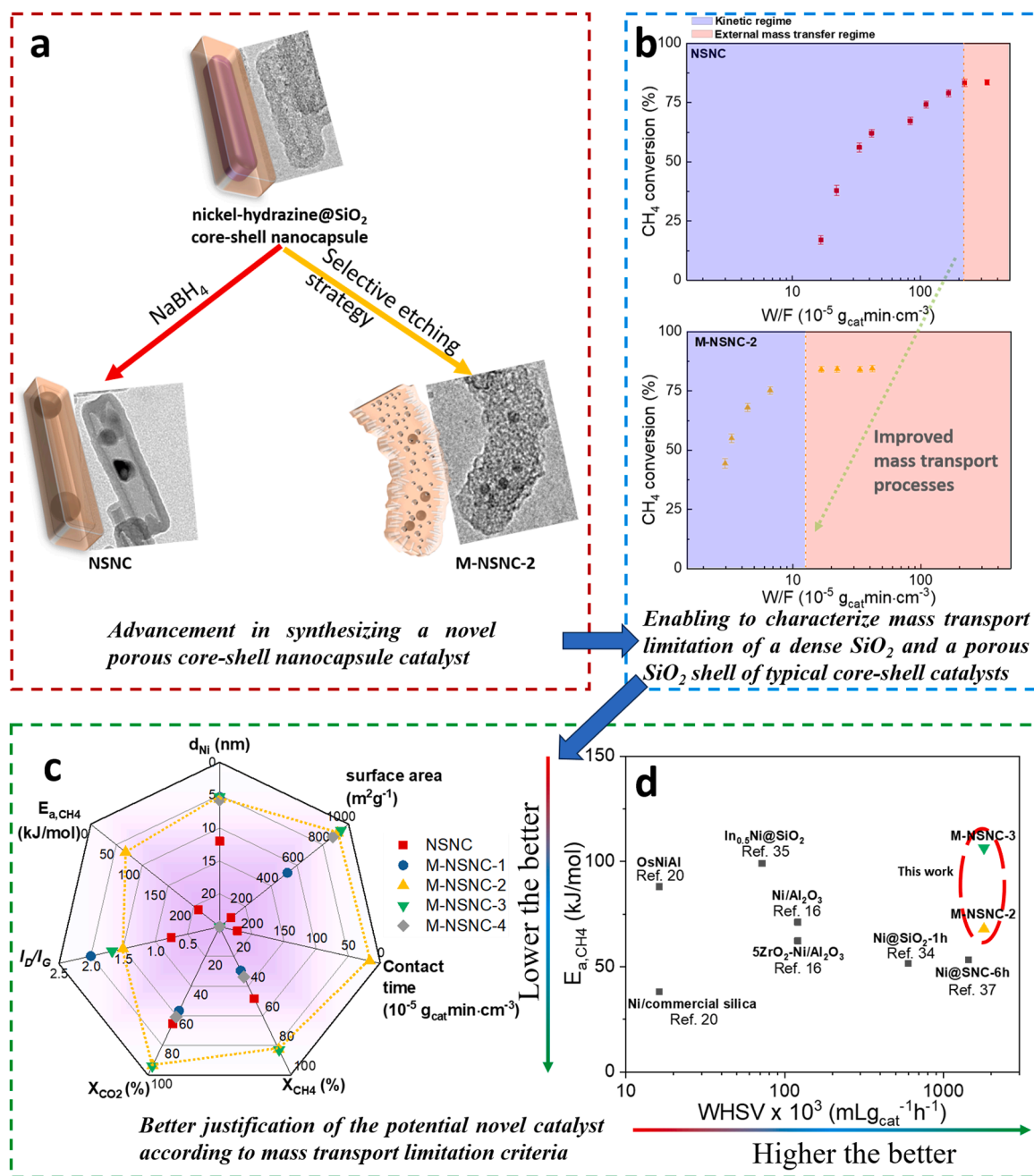
Fig. 10. The illustrations of developed dense SiO_2 and porous SiO_2 nanocapsule catalysts (a), their difference in diffusion capability (b), overall performance and characteristic of the catalysts for dry reforming of methane (c), and the reported apparent CH_4 activation energy (d).

interests or personal relationships that could have appeared to influence the work reported in this paper.

Data availability

No data was used for the research described in the article.

Appendix A. Supporting information

Supplementary data associated with this article can be found in the online version at doi:10.1016/j.apcatb.2024.123891.

References

[1] Z. Liu, Z. Deng, S.J. Davis, C. Giron, P. Ciais, Monitoring global carbon emissions in 2021, Nat. Rev. Earth Environ. 3 (2022) 217–219.
[2] R. Newell, D. Raimi, G. Aldana, Global energy outlook 2019: the next generation of energy, Resources for the Future, 1 (2019) 8-19.
[3] R.J. Lowe, P. Drummond, Solar, wind and logistic substitution in global energy supply to 2050 – Barriers and implications, Renew. Sustain. Energy Rev. 153 (2022) 111720.
[4] J.E.T. Bistline, G.J. Blanford, Impact of carbon dioxide removal technologies on deep decarbonization of the electric power sector, Nature, Communications 12 (2021) 3732.

[5] S. Peng, X. Lin, R.L. Thompson, Y. Xi, G. Liu, D. Hauglustaine, X. Lan, B. Poulter, M. Ramonet, M. Saunois, Y. Yin, Z. Zhang, B. Zheng, P. Ciais, Wetland emission and atmospheric sink changes explain methane growth in 2020, Nature 612 (2022) 477–482.

[6] C.-f Li, R.-t Guo, Z.-r Zhang, T. Wu, W.-g Pan, Converting CO2 into Value-Added Products by Cu2O-Based Catalysts: From Photocatalysis, Electrocatalysis to Photoelectrocatalysis, n/a 2207875.

[7] J.-L. Zheng, Y.-H. Zhu, G.-T. Sun, Y.-Y. Dong, M.-Q. Zhu, Bio-oil gasification for production of the raw gas as ammonia syngas, Fuel 327 (2022) 125029.

[8] X. Pan, F. Jiao, D. Miao, X. Bao, Oxide–zeolite-based composite catalyst concept that enables syngas chemistry beyond fischer–tropsch synthesis, Chem. Rev. 121 (2021) 6588–6609.

[9] N.A.K. Aramouni, J.G. Touma, B.A. Tarboush, J. Zeaiter, M.N. Ahmad, Catalyst design for dry reforming of methane: analysis review, Renew. Sustain. Energy Rev. 82 (2018) 2570–2585.

[10] J. Sehested, Four challenges for nickel steam-reforming catalysts, Catal. Today 111 (2006) 103–110.

[11] J.J. Torrez-Herrera, S.A. Korili, A. Gil, Recent progress in the application of Ni-based catalysts for the dry reforming of methane, Catal. Rev. (2021) 1–58.

[12] L. Wang, F. Wang, Design Strategy, Synthesis, and Mechanism of Ni Catalysts for Methane Dry Reforming Reaction: Recent Advances and Future Perspectives, Energy & Fuels, 36 (2022) 5594-5621.

[13] Z. Alipour, V. Babu Borugadda, H. Wang, A.K. Dalai, Syngas production through dry reforming: a review on catalysts and their materials, preparation methods and reactor type, Chem. Eng. J. 452 (2023) 139416.

[14] D. Duprez, M.C. DeMicheli, P. Marecot, J. Barbier, O.A. Ferretti, E.N. Ponzi, Deactivation of steam-reforming model catalysts by coke formation: I. Kinetics of the formation of filamentous carbon in the hydrogenolysis of Cyclopentane on Ni/Al2O3 catalysts, J. Catal. 124 (1990) 324–335.

[15] T.G. de Araújo Moreira, J.F.S. de Carvalho Filho, Y. Carvalho, J.M.A.R. de Almeida, P. Nothaft Romano, E. Falabella, Sousa-aguiar, highly stable low noble metal content rhodium-based catalyst for the dry reforming of methane, Fuel 287 (2021) 119536.

[16] B. Jin, S. Li, Y. Liu, X. Liang, Engineering metal-oxide interface by depositing ZrO2 overcoating on Ni/Al2O3 for dry reforming of methane, Chem. Eng. J. 436 (2022) 135195.

[17] B. Jin, S. Li, X. Liang, Enhanced activity and stability of MgO-promoted Ni/Al2O3 catalyst for dry reforming of methane: role of MgO, Fuel 284 (2021) 119082.

[18] M. Rezaei, S.M. Alavi, S. Sahebdelfar, Z.-F. Yan, Effects of K 2O promoter on the activity and stability of nickel catalysts supported on mesoporous nanocrystalline zirconia in CH 4 reforming with CO 2, Energy Fuels 22 (2008) 2195–2202.

[19] Y. Han, M. Tian, C. Wang, Y. Kang, L. Kang, Y. Su, C. Huang, T. Zong, J. Lin, B. Hou, X. Pan, X. Wang, Highly active and anticoke Ni/CeO2 with ultralow ni loading in chemical looping dry reforming via the strong metal–support interaction, ACS Sustain. Chem. Eng. 9 (2021) 17276–17288.

[20] S. Das, M. Sengupta, J. Patel, A. Bordoloi, A study of the synergy between support surface properties and catalyst deactivation for CO2 reforming over supported Ni nanoparticles, Appl. Catal. A Gen. 545 (2017) 113–126.

[21] D. Sastre, C.Á. Galván, P. Pizarro, J.M. Coronado, Enhanced performance of CH4 dry reforming over La0.9Sr0.1FeO3/YSZ under chemical looping conditions, Fuel 309 (2022) 122122.

[22] Z. Zhang, G. Zhao, G. Bi, Y. Guo, J. Xie, Monolithic SiC-foam supported Ni-La2O3 composites for dry reforming of methane with enhanced carbon resistance, Fuel Process. Technol. 212 (2021) 106627.

[23] Y. Diao, H. Wang, B. Chen, L. Wang, X. Zhang, C. Shi, Ordered mesoporous Ni-La2O3/Al2O3 catalysts towards efficient plasma-assisted dry reforming of methane, Fuel Process. Technol. 243 (2023) 107676.

[24] Q. Song, R. Ran, X. Wu, Z. Si, D. Weng, Dry reforming of methane over Ni catalysts supported on micro- and mesoporous silica, J. CO2 Util. 68 (2023) 102387.

[25] M. Rezaei, S.M. Alavi, S. Sahebdelfar, L. Xinmei, L. Qian, Z.-F. Yan, CO2−CH4 reforming over nickel catalysts supported on mesoporous nanocrystalline zirconia with high surface area, Energy Fuels 21 (2007) 581–589.

[26] Z. Wang, J. Qi, N. Yang, R. Yu, D. Wang, Core–shell nano/microstructures for heterogeneous tandem catalysis, Mater. Chem. Front. 5 (2021) 1126–1139.

[27] Z.-Y. Lim, C. Wu, W.G. Wang, K.-L. Choy, H. Yin, A novel and anti-agglomerating Ni@yolk–ZrO2 structure with sub-10 nm Ni core for high performance steam reforming of methane, RSC Adv. 5 (2015) 61925–61932.

[28] Z.-Y. Lim, C. Wu, W.G. Wang, K.-L. Choy, H. Yin, Porosity effect on ZrO2 hollow shells and hydrothermal stability for catalytic steam reforming of methane, J. Mater. Chem. A 4 (2016) 153–159.

[29] Y. Shi, K. Han, F. Wang, Ni−Cu Alloy Nanoparticles confined by physical encapsulation with SiO2 and chemical metal–support interaction with CeO2 for methane dry reforming, Inorg. Chem. 61 (2022) 15619–15628.

[30] W. Wang, L. He, Q. Luo, L. Wang, J. Wang, H. Chen, Z. Miao, Q. Yao, M. Sun, Synthesis and application of core-shell, hollow, yolk-shell multifunctional structure zeolites, Microporous Mesoporous Mater. 362 (2023) 112766.

[31] M. Kaviani, M. Rezaei, S.M. Alavi, E. Akbari, Biogas dry reforming over nickel-silica sandwiched core–shell catalysts with various shell thicknesses, Fuel 355 (2024) 129533.

[32] Z.-Y. Lim, J. Tu, F. Zhou, Y. Xu, B. Chen, Anti-coking Ni encapsulated in SiO2 via one-pot reverse microemulsion method as a versatile catalyst for CO2 methane reforming, J. CO2 Util. 67 (2023) 102341.

[33] J. Liu, S.Z. Qiao, J.S. Chen, X.W. Lou, X. Xing, G.Q. Lu, Yolk/shell nanoparticles: new platforms for nanoreactors, drug delivery and lithium-ion batteries, Chem. Commun. 47 (2011) 12578–12591.

[34] F. Wang, B. Han, L. Zhang, L. Xu, H. Yu, W. Shi, CO2 reform. methane small-sized Ni@SiO2 Catal. unique features sinter. free low. carbon, Appl. Catal. B: Environ. 235 (2018) 26–35.

[35] W. Liu, L. Li, S. Lin, Y. Luo, Z. Bao, Y. Mao, K. Li, D. Wu, H. Peng, Confined Ni-In intermetallic alloy nanocatalyst with excellent coking resistance for methane dry reforming, J. Energy Chem. 65 (2022) 34–47.

[36] M. Kaviani, M. Rezaei, S. Mehdi Alavi, E. Akbari, High coke resistance Ni-SiO2@ SiO2 core-shell catalyst for biogas dry reforming: effects of Ni loading and calcination temperature, Fuel 330 (2022) 125609.

[37] C. Wang, X. Jie, Y. Qiu, Y. Zhao, H.A. Al-Megren, S. Alshihri, P.P. Edwards, T. Xiao, Import. Inn. cavity Space Ni@SiO2 nanocapsule Catal. Excell. coking Resist. High. -Space-Veloc. Dry. Reform. methane, Appl. Catal. B: Environ. 259 (2019) 118019.

[38] Z.-Y. Lim, J. Tu, Y. Xu, B. Chen, Enhanced porosity of Ni@Hollow meso-SiO2 catalyst for CO2 reforming of methane, Int. J. Hydrog. Energy 46 (2021) 7866–7877.

[39] Z. Bian, S. Deng, Z. Sun, T. Ge, B. Jiang, W. Zhong, Multi-core@Shell catalyst derived from LDH@SiO2 for low- temperature dry reforming of methane, Renew. Energy 200 (2022) 1362–1370.

[40] Y. Liu, Y. Chen, Z. Gao, X. Zhang, L. Zhang, M. Wang, B. Chen, Y. Diao, Y. Li, D. Xiao, X. Wang, D. Ma, C. Shi, Embed. High. Load. Unif. Ni Nanopart. into silicalite-1 zeolite Dry. Reform. methane, Appl. Catal. B: Environ. 307 (2022) 121202.

[41] J. Pu, K. Nishikado, N. Wang, T.T. Nguyen, T. Maki, E.W. Qian, Core-Shell Nickel Catal. Steam. Reform. acetic Acid., Appl. Catal. B: Environ. 224 (2018) 69–79.

[42] J. Wang, Y. Fu, W. Kong, F. Jin, J. Bai, J. Zhang, Y. Sun, Des. a Carbon-Resist. Ni@S-2 Reform. Catal.: Control. Ni Nanopart. Sandw. a peasecod- Struct., Appl. Catal. B: Environ. 282 (2021) 119546.

[43] C. Wang, H. Wu, X. Jie, X. Zhang, Y. Zhao, B. Yao, T. Xiao, Yolk–Shell Nanocapsule Catal. Nanoreactors Var. Shell Struct. Their Diffus. Eff. CO2 Reform. Methane, ACS Appl. Mater. Interfaces 13 (2021) 31699–31709.

[44] C. Gao, Z. Lu, Y. Yin, Gram-scale synthesis of silica nanotubes with controlled aspect ratios by templating of nickel-hydrazine complex nanorods, Langmuir 27 (2011) 12201–12208.

[45] Y. Wang, H. Wang, A.H. Dam, L. Xiao, Y. Qi, J. Niu, J. Yang, Y.-A. Zhu, A. Holmen, D. Chen, Understanding effects of Ni particle size on steam methane reforming activity by combined experimental and theoretical analysis, Catal. Today 355 (2020) 139–147.

[46] F. Pompeo, N.N. Nichio, M.M.V.M. Souza, D.V. Cesar, O.A. Ferretti, M. Schmal, Study of Ni and Pt catalysts supported on α-Al2O3 and ZrO2 applied in methane reforming with CO2, Appl. Catal. A: Gen. 316 (2007) 175–183.

[47] C. Perego, S. Peratello, Experimental methods in catalytic kinetics, Catal. Today 52 (1999) 133–145.

[48] M.H. Al-Dahhan, Y. Wu, M.P. Dudukovic, Reproducible technique for packing laboratory-scale trickle-bed reactors with a mixture of catalyst and fines, Ind. Eng. Chem. Res. 34 (1995) 741–747.

[49] V.G. de la Cruz-Flores, A. Martinez-Hernandez, M.A. Gracia-Pinilla, Deactivation of Ni-SiO2 catalysts that are synthetized via a modified direct synthesis method during the dry reforming of methane, Appl. Catal. A Gen. 594 (2020) 117455.

[50] L. Zhou, L. Li, N. Wei, J. Li, J.-M. Basset, Effect of NiAl2O4 Formation on Ni/Al2O3 Stability during dry reforming of methane 7 (2015) 2508–2516.

[51] M. Ghelamallah, P. Granger, Impact of barium and lanthanum incorporation to supported Pt and Rh on α-Al2O3 in the dry reforming of methane, Fuel 97 (2012) 269–276.

[52] J.-H. Park, S. Yeo, T.-S. Chang, Effect of supports on the performance of Co-based catalysts in methane dry reforming, J. CO2 Util. 26 (2018) 465–475.

[53] N.H. Elsayed, N.R.M. Roberts, B. Joseph, J.N. Kuhn, Low. Temp. Dry. Reform. methane Pt–Ni–Mg/Ceria-zirconia Catal., Appl. Catal. B: Environ. 179 (2015) 213–219.

[54] X. Fang, X. Chen, Z. Liu, P. Liu, N. Zheng, A cationic surfactant assisted selective etching strategy to hollow mesoporous silica spheres, Nanoscale 3 (2011) 1632–1639.

[55] Z.-Y. Lim, J. Tu, Y. Xu, B. Chen, Ni@ZrO2 yolk-shell catalyst for CO2 methane reforming: effect of Ni@SiO2 size as the hard-template, J. Colloid Interface Sci. 590 (2021) 641–651.

[56] R. Mokaya, Hydrothermally stable restructured mesoporous silica, Chem. Commun. (2001) 933–934.

[57] M. Thommes, K. Kaneko, A.V. Neimark, J.P. Olivier, F. Rodriguez-Reinoso, J. Rouquerol, K.S.W. Sing, Physisorption of gases, with special reference to the evaluation of surface area and pore size distribution (IUPAC Technical Report) %J, Pure Appl. Chem. 87 (2015) 1051–1069.

[58] L.F. Lundegaard, R.R. Tiruvalam, C. Tyrsted, A. Carlsson, F. Morales-Cano, C.V. Ovesen, Migrating Al species hindering NiO reduction on Al containing catalyst carriers, Catal. Today 272 (2016) 25–31.

[59] K. Han, S. Wang, N. Hu, W. Shi, F. Wang, Alloy. Ni–Cu Nanopart. Encapsulated SiO2 Nanospheres Synerg. Catal. CO2 Reform. Methane React., ACS Appl. Mater. Interfaces 14 (2022) 23487–23495.

[60] Z. Zhou, S. Sarmad, C. Huang, G. Deng, Z. Sun, L. Duan, Ni-based catalyst supported on ordered mesoporous Al2O3 for dry CH4 reforming: effect of the pore structure, Int. J. Hydrog. Energy 52 (2024) 275–288.

[61] B. Li, X. Yuan, B. Li, X. Wang, Impact of pore structure on hydroxyapatite supported nickel catalysts (Ni/HAP) for dry reforming of methane, Fuel Process. Technol. 202 (2020) 106359.

[62] Q. Zhang, X. Feng, J. Liu, L. Zhao, X. Song, P. Zhang, L. Gao, Hollow hierarchical Ni/MgO-SiO2 catalyst with high activity, thermal stability and coking resistance for catalytic dry reforming of methane, Int. J. Hydrog. Energy 43 (2018) 11056–11068.

[63] Y. Shi, L. Wang, M. Wu, F. Wang, Order-of-magnitude increase in rate of methane dry reforming over Ni/CeO2-SiC catalysts by microwave catalysis, applied catalysis B: environmental 337 (2023) 122927.

[64] B. Baumgartner, J. Hayden, J. Loizillon, S. Steinbacher, D. Grosso, B. Lendl, Pore Size-dependent structure of confined water in mesoporous silica films from water adsorption/desorption using ATR–FTIR spectroscopy, Langmuir 35 (2019) 11986–11994.

[65] L. Wang, Z. Pu, Y. Shi, M. Wu, W. Shi, F. Wang, Photo Methane Dry. Reform. Catalyzed Multifunct. (Ni–Cu/CeO2)@SiO2 Catal., ACS Sustain. Chem. Eng. 11 (2023) 17384–17399.

[66] Z. Bao, Z. Lu, J. Han, Y. Li, F. Yu, Highly active and stable Ni-based bimodal pore catalyst for dry reforming of methane, Appl. Catal. A Gen. 491 (2015) 116–126.

[67] H. Qiu, J. Ran, X. Huang, Z. Ou, J. Niu, Unrevealing the influence that preparation and reaction parameters have on Ni/Al2O3 catalysts for dry reforming of methane, Int. J. Hydrog. Energy 47 (2022) 34066–34074.

[68] K.Y. Koo, S.-h Lee, U.H. Jung, H.-S. Roh, W.L. Yoon, Syngas production via combined steam and carbon dioxide reforming of methane over Ni–Ce/MgAl2O4 catalysts with enhanced coke resistance, Fuel Process. Technol. 119 (2014) 151–157.

[69] L. Lyu, M. Shengene, Q. Ma, J. Sun, X. Gao, H. Fan, J. Zhang, T.-S. Zhao, Synergy of macro-meso bimodal pore and Ni-Co alloy for enhanced stability in dry reforming of methane, Fuel 310 (2022) 122375.

[70] Z. Li, L. Deng, I.A. Kinloch, R.J. Young, Raman spectroscopy of carbon materials and their composites: graphene, nanotubes and fibres, Prog. Mater. Sci. 135 (2023) 101089.

[71] V. Țucureanu, A. Matei, A.M. Avram, FTIR Spectroscopy for Carbon Family Study, Crit. Rev. Anal. Chem. 46 (2016) 502–520.

[72] L. Guczi, G. Stefler, O. Geszti, I. Sajó, Z. Pászti, A. Tompos, Z. Schay, Methane dry reforming with CO2: a study on surface carbon species, Appl. Catal. A: Gen. 375 (2010) 236–246.

[73] J.H. Yang, H.-J. Kim, D.H. Chun, H.-T. Lee, J.-C. Hong, H. Jung, J.-I. Yang, Mass transfer limitations on fixed-bed reactor for fischer–tropsch synthesis, Fuel Process. Technol. 91 (2010) 285–289.

[74] J.A. Dumesic, G.W. Huber, M. Boudart, Principles of Heterogeneous Catalysis, Handbook of Heterogeneous Catalysis.

[75] J. Wei, E. Iglesia, Isotopic and kinetic assessment of the mechanism of reactions of CH4 with CO2 or H2O to form synthesis gas and carbon on nickel catalysts, J. Catal. 224 (2004) 370–383.

[76] M.C.J. Bradford, M.A. Vannice, CO2 Reforming of CH4, Catal. Rev. 41 (1999) 1–42.

[77] Z. Xie, B. Yan, S. Kattel, J.H. Lee, S. Yao, Q. Wu, N. Rui, E. Gomez, Z. Liu, W. Xu, L. Zhang, J.G. Chen, Dry. Reform. methane CeO2-Support. Pt-Co. Catal. Enhanc. Act., Appl. Catal. B: Environ. 236 (2018) 280–293.

[78] C. Chen, X. Wang, L. Zhang, X. Zou, W. Ding, X. Lu, Synthesis of mesoporous Ni–La2O3/SiO2 by ploy(ethylene glycol)-assisted sol-gel route as highly efficient catalysts for dry reforming of methane with a H2/CO ratio of unity, Catal. Commun. 94 (2017) 38–41.

[79] K.A. Dahlberg, J.W. Schwank, Synthesis of Ni@SiO2 nanotube particles in a Water-in-oil microemulsion template, Chem. Mater. 24 (2012) 2635–2644.

[80] C. Wang, Y. Qiu, X. Zhang, Y. Zhang, N. Sun, Y. Zhao, Geometric design of a Ni@ silica nano-capsule catalyst with superb methane dry reforming stability: enhanced confinement effect over the nickel site anchoring inside a capsule shell with an appropriate inner cavity, Catal. Sci. Technol. 8 (2018) 4877–4890.

[81] T.K. Lim, Pisum sativum, in: T.K. Lim (Ed.) Edible Medicinal And Non-Medicinal Plants: Volume 2, Fruits, Springer Netherlands, Dordrecht, 2012, pp. 849-866.

[82] X. Fang, Z. Liu, M.-F. Hsieh, M. Chen, P. Liu, C. Chen, N. Zheng, Hollow mesoporous aluminosilica spheres with perpendicular pore channels as catalytic nanoreactors, ACS Nano 6 (2012) 4434–4444.

[83] E.B. Abuin, M.A. Rubio, E.A. Lissi, Solubility of water in water-in-oil microemulsions stabilized by cetyltrimethylammonium: effects of the surfactant counterion, the nature and composition of the oil, and the salinity of the droplets, J. Colloid Interface Sci. 158 (1993) 129–132.

[84] W. Yang, J. Chen, J. Tu, Z.-Y. Lim, B. Chen, A porous ni@SiO2 nanocatalysts for CO2 methane reforming 8 (2023) e202203080.

[85] Z. Liu, R. Che, A.A. Elzatahry, D. Zhao, Direct I, ACS Nano 8 (2014) 10455–10460. Maging Au Nanoparticle Migration inside Mesoporous Silica Channels,.

[86] C. Byron, M.S. Ferrandon, A.J. Kropf, M. Delferro, A.V. Teplyakov, Surface basic site effect on boron-promoted platinum catalysts for dry reforming of methane, the, J. Phys. Chem. C. 127 (2023) 24137–24148.

[87] M.A. Ashraf, O. Sanz, C. Italiano, A. Vita, M. Montes, S. Specchia, Analysis of Ru/La-Al2O3 catalyst loading on alumina monoliths and controlling regimes in methane steam reforming, Chem. Eng. J. 334 (2018) 1792–1807.